

Molecular Gas Detections in Eight Faint DSFGs with Red NIR Colors at $z \sim 1.2 - 2.5$

MICHAEL J. NICANDRO ROSENTHAL,¹ STEPHEN J. MCKAY,² AMY J. BARGER,^{1,3,4} AND LENNOX L. COWIE⁴

¹Department of Astronomy, University of Wisconsin–Madison, 475 N. Charter Street, Madison, WI 53706, USA

²Department of Physics, University of Wisconsin–Madison, 475 N. Charter Street, Madison, WI 53706, USA

³Department of Physics and Astronomy, University of Hawaii, 2505 Correa Road, Honolulu, HI 96822, USA

⁴Institute for Astronomy, University of Hawaii, 2680 Woodlawn Drive, Honolulu, HI 96822, USA

Submitted to ApJ

ABSTRACT

We present a NOEMA survey of CO(3–2), CO(4–3), and [C I] (${}^3\text{P}_1 - {}^3\text{P}_0$) in eight faint (average $S_{850\mu\text{m}} = 2.3 \text{ mJy}$) dusty star-forming galaxies (DSFGs) at $z = 1.2 - 2.5$. We used a NIR flux-color cut to match faint SCUBA-2 sources to red stellar counterparts with existing spectroscopic redshifts, allowing us to target CO lines at known frequencies. We obtained seven new CO detections and a serendipitous [C I] detection in an off-axis source, and measured molecular gas masses of $M_{\text{mol}} = (6 - 22) \times 10^{10} (\alpha_{\text{CO}}/3.6) M_{\odot}$ from these lines. We performed UV-to-mm SED fits to measure the SFRs and stellar masses of our sample, and compared these with two other $z = 1 - 3$ CO samples from the literature. The CO detections have constant depletion times of $t_{\text{dep}} \sim 500 \text{ Myr}$, with no evidence for correlation between t_{dep} and redshift or main-sequence offset. We find that low-mass ($M_{\star} \lesssim 10^{11} M_{\odot}$), starbursting galaxies have gas fractions and depletion times twice as high as predicted by molecular gas scaling relations, which may indicate that M_{mol} is systematically over-estimated in this population, possibly due to decreased α_{CO} or increased CO excitation compared to the well-studied massive and/or main-sequence DSFG population.

Keywords: Submillimeter astronomy (1647) — Molecular gas (1073) — Galaxy evolution (594)

1. INTRODUCTION

Roughly half of the star formation across cosmic time is obscured by dust (e.g., P. Madau & M. Dickinson 2014; J. A. Zavala et al. 2021) and re-radiated at submillimeter/millimeter (submm/mm) wavelengths. While the brightest dusty star-forming galaxies (DSFGs) have the highest individual star formation rates (SFRs) of any galaxies, the majority of dust-obscured star formation since $z \sim 2$ has occurred in relatively faint ($S_{850\mu\text{m}} \lesssim 2 \text{ mJy}$) DSFGs, which are far more numerous and account for the majority of the total infrared extragalactic background light (e.g., C.-C. Chen et al. 2013; L.-Y. Hsu et al. 2016; Q. N. Hsu et al. 2024). Measuring the molecular gas content fueling star formation in faint DSFGs is thus a critical component of understanding the processes governing the Universe’s star formation history (SFH) as a whole.

Corresponding author: Michael J. Nicandro Rosenthal
 rosenthal@astro.wisc.edu

The molecular gas masses (M_{mol}) of star-forming galaxies are best measured by observing the rotational emission lines of CO (e.g., T. R. Greve et al. 2005; P. M. Solomon & P. A. Vanden Bout 2005; M. S. Bothwell et al. 2013; L. J. Tacconi et al. 2013, 2018; M. Aravena et al. 2019, hereafter A19; J. E. Birkin et al. 2021, hereafter B21), chiefly with millimeter interferometers, such as the Northern Extended Millimeter Array (NOEMA) and the Atacama Large Millimeter/submillimeter Array (ALMA). Such surveys have shown that the luminosities of CO lines (L'_{CO}) scale monotonically with integrated infrared luminosity (L_{IR} , e.g., M. S. Bothwell et al. 2013; D. Liu et al. 2015) at all redshifts, reflecting the fundamental relationship between SFR (traced by L_{IR}) and M_{mol} (M. Schmidt 1959; R. C. Kennicutt 1998). Recent works have compiled thousands of CO detections to fit measured molecular gas scaling relations (see L. J. Tacconi et al. 2020, hereafter T20, for a review) finding galaxies to be more gas-rich at higher redshifts and lower stellar masses; they also have shorter depletion times ($t_{\text{dep}} \equiv M_{\text{mol}}/\text{SFR}$)

the higher they are above the star-forming main sequence (SFMS).

Most of these CO surveys, however, are biased toward the brightest, most highly star-forming DSFGs due to their sample selection, especially at $z \gtrsim 1$, since most CO-detected DSFGs have been selected from single-dish submm/mm imaging, and submm/mm flux is directly related to SFR (e.g., A. J. Barger et al. 2014; L. L. Cowie et al. 2017). Single-dish telescopes are fundamentally limited by confusion noise (e.g., A. W. Blain et al. 1998), such that almost all single-dish sources have SFR $\gtrsim 100 \text{ M}_\odot \text{ yr}^{-1}$.

An alternative approach is to obtain deep, wide-bandwidth observations over mosaicked fields, and thus forgo target selection altogether. The most sensitive such survey is the ALMA Spectroscopic Survey in the Hubble Ultra Deep Field (ASPECS; F. Walter et al. 2016; A19), an ALMA large program that obtained uniform 3 mm sensitivity across a 5 arcmin² survey area. They detected CO emission in 18 galaxies, which spanned a wider range of stellar masses, SFRs, and SFMS offsets than those in pre-selected CO surveys (A19). While successfully circumventing the biases associated with pre-selected DSFG samples, this approach is extremely inefficient compared to targeted CO surveys. Global inferences about the molecular gas properties of faint DSFGs inferred from surveys such as this are limited both by the small sample size and by potential bias due to cosmic variance, given the small survey area. Constructing large samples of CO in faint DSFGs over larger areas is therefore necessary to characterize properly the CO in the faint DSFG population.

In this work, we present a pilot survey with NOEMA that uses a targeted approach but leverages the deepest available single-dish imaging and pre-JWST optical/infrared (OIR) spectroscopy to restrict our sample to galaxies with low L_{IR} . We select the faintest sources from confusion-limited imaging with the Submillimeter Common-User Bolometer Array 2 (SCUBA-2; W. S. Holland et al. 2013) and employ a near-infrared (NIR) color selection to determine accurately the OIR counterparts to the faintest SCUBA-2 sources (A. J. Barger & L. L. Cowie 2023; S. J. McKay et al. 2024). We use this counterpart selection to also target only DSFGs with known spectroscopic redshifts, greatly improving the efficiency of our survey compared to deep, blind surveys like ASPECS.

We organize the paper as follows: In Section 2, we describe our sample selection and observing strategy, including the NIR color selection we use to identify OIR counterparts with existing spectroscopic redshifts. We describe our 2 mm NOEMA observations, data reduction, and analysis of the line and continuum emission in Section 3, and the results of this analysis in Section 4. We derive the physical properties of our sample in Section 5, including deriving molecular gas masses from our observed CO and [C I] lines. Fi-

nally, in Section 6, we compare our CO sample with several larger CO surveys using ALMA and NOEMA and with predictions from molecular gas scaling relations, and we discuss prospects for future surveys of molecular gas that leverage NIR color selection. We summarize the paper in Section 7.

All calculations throughout this work assume a concordance flat Λ CDM cosmology with $H_0 = 70 \text{ km s}^{-1} \text{ Mpc}^{-1}$, $\Omega_{\text{m},0} = 0.3$, and $\Omega_{\Lambda,0} = 0.7$. Masses and SFRs are scaled to a G. Chabrier (2003) initial mass function (IMF) unless otherwise stated. All magnitudes are in the AB system.

2. DATA AND SAMPLE SELECTION

2.1. Confusion-Limited SCUBA-2 Imaging

To select faint DSFGs, we use the 850 μm source catalog from the Submillimeter Perspective on the GOODS Fields (SUPER GOODS) survey of the GOODS-N (L. L. Cowie et al. 2017) as our parent DSFG sample. This imaging covers an area of ~ 400 arcmin² centered on the 2 Ms *Chandra* image (D. M. Alexander et al. 2003) and the original HST GOODS-N field (M. Giavalisco et al. 2004). It includes a circular region of radius $\sim 4'$ (area ~ 50 arcmin²) where the instrumental noise reaches the confusion limit, such that the faintest 4σ detections have fluxes of only $S_{850\mu\text{m}} = 1.4 \text{ mJy}$. These are the faintest DSFGs that can be detected by SCUBA-2 without gravitational lensing (e.g., Cowie et al. 2022).

2.2. Ancillary OIR Photometry and Spectroscopy

For OIR data, we use the multiwavelength photometric catalog of G. Barro et al. (2019). This catalog uses the HST/Wide Field Camera 3 (WFC3) F160W image from the Cosmic Assembly Near-infrared Deep Extragalactic Legacy Survey (CANDELS; N. A. Grogin et al. 2011; A. M. Koekemoer et al. 2011) for source detection, reaching a 5σ limiting magnitude of F160W = 27.3 across a survey area of 171 arcmin² centered on the GOODS-N. It includes photometry in 23 broadband filters from UV to far-infrared (FIR) wavelengths and contains 33,961 secure galaxy detections, i.e., objects that were not flagged as having poor data quality and not classified as stars. The CANDELS high-level science products¹ also include a spectroscopic catalog, which was compiled from a variety of spectroscopic surveys of the GOODS-N. In this work, we use the v2 spectroscopic catalog from D. Kodra et al. (2023), which contains 3206 spectroscopic redshifts.

2.3. Red Selection to Identify Counterparts to DSFGs

Mid-infrared (MIR; e.g., Pope et al. 2006) or radio (e.g., Barger et al. 2012) sources have been used for counterpart matching to DSFGs in the past. However, since the advent of

¹ <https://archive.stsci.edu/hlsp/candels>

JWST, focus has turned to using red sources. [A. J. Barger & L. L. Cowie \(2023\)](#) found that a simple JWST/NIRCam selection of $f_{\text{F444W}} > 1 \mu\text{Jy}$ and $f_{\text{F444W}}/f_{\text{F150W}} > 3.5$ identified the ALMA counterparts of most SCUBA-2 sources; [S. J. McKay et al. \(2024\)](#) later showed this selection to be $\sim 95\%$ accurate. The unprecedented depth of NIRCam means that the number of DSFGs that can be identified this way far exceeds the number with MIR or radio counterparts, as well as having better spatial resolution and being less susceptible to active galactic nucleus (AGN) contamination than most MIR or radio priors. This makes NIR color selection especially promising for the study of faint, lower-mass DSFGs (e.g. [S. J. McKay et al. 2025](#); [L. Barrufet et al. 2025](#)).

In this work, we match the SUPER GOODS sources with their CANDELS counterparts by using a NIR color selection with the Spitzer/IRAC 4.5 μm (hereafter IRAC2) and HST/WFC3 F160W filters:

$$f_{\text{IRAC2}} \geq 1 \mu\text{Jy} \wedge \frac{f_{\text{IRAC2}}}{f_{\text{F160W}}} > 3.5. \quad (1)$$

We hereafter refer to this as our *red selection*. This selection was chosen to be analogous to the NIRCam selection of [A. J. Barger & L. L. Cowie \(2023\)](#).

In Figure 1, we plot all of the [G. Barro et al. \(2019\)](#) galaxies that lie within 5'' of a SUPER GOODS 850 μm source, with our red selection shown by the red lines. This 5'' radius is motivated by ALMA follow-up of SCUBA-2 sources in the GOODS-S by [L. L. Cowie et al. \(2018\)](#), who found that $>90\%$ of SCUBA-2 sources have at least one ALMA counterpart within this radius. We mark the 22 CANDELS galaxies within 1'' of an 860 μm Submillimeter Array (SMA) position from [L. L. Cowie et al. \(2017\)](#) with open blue circles; 20/22 (91%) of these satisfy our red selection.

We note that while the red selection we employ is similar to the “H-IRAC Extremely Red Object” (“HIERO”; [T. Wang et al. 2016, 2019](#)) criterion ($\text{F160W} - \text{IRAC2} < 2.25$ mag, or $f_{\text{IRAC2}}/f_{\text{F160W}} > 7.9$), our inclusion of galaxies with less red colors, that is, $3.5 \leq f_{\text{IRAC2}}/f_{\text{F160W}} \leq 7.9$, is better at selecting the OIR counterparts of less massive and/or less dusty DSFGs at $z < 3$ ([S. J. McKay et al. 2025](#)). This is demonstrated by the fact that 8/22 of the open blue circles (and 6/8 of the targets in this work; see Section 2.4) are not HIEROs but are selected by our method.

In total, 127 CANDELS galaxies satisfy our red selection and fall within 5'' of a SCUBA-2 source, making them likely OIR counterparts to the submm sources. These galaxies are shown in Figure 1 as red circles, and we select our NOEMA targets from this subsample.

2.4. NOEMA Targets

These 127 red-selected CANDELS galaxies are matched to 90 unique SCUBA-2 sources. This average multiplicity of 1.4 is consistent with the number of ALMA counterparts

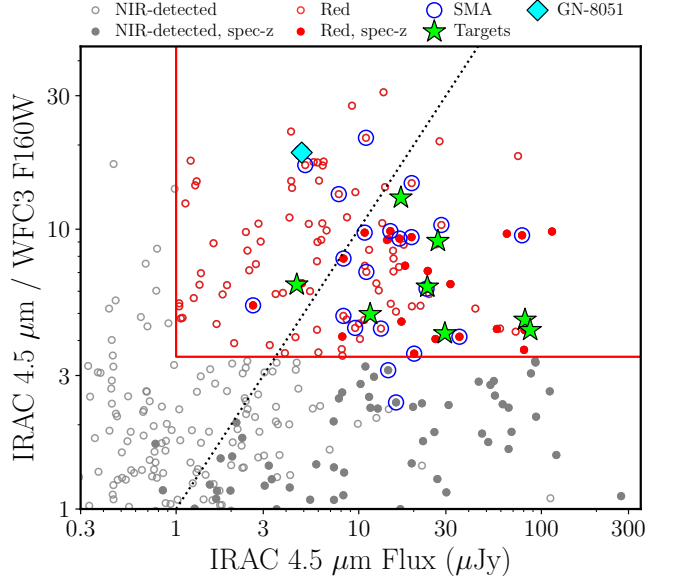


Figure 1. HST/WFC3 F160W and Spitzer/IRAC 4.5 μm color-magnitude diagram showing the criterion used for our sample selection. The circles in this figure are [G. Barro et al. \(2019\)](#) CANDELS galaxies within 5'' of a [L. L. Cowie et al. \(2017\)](#) 850 μm position. The red solid lines show our red selection (Equation 1), with red and gray points showing galaxies that do and do not satisfy this selection, respectively. Filled and open circles are points with and without spectroscopic redshifts, respectively. The large blue circles show CANDELS galaxies within 1'' of an SMA position from [L. L. Cowie et al. \(2017\)](#). Our NOEMA targets are shown as green stars, while the cyan diamond shows the serendipitous detection GN-8051 (see Section 4.1). The black dotted line shows an arbitrary cutoff of 1 μJy (23.9 AB mag) in F160W, below which very few sources have spectroscopic redshifts.

per SCUBA-2 source found by [L. L. Cowie et al. \(2018\)](#) in the GOODS-S, and suggests of the SCUBA-2 sources may be blends of multiple DSFGs. We limit our sample to only those sources with 1-to-1 matches between red-selected CANDELS galaxies and SCUBA-2 sources. We also require a spectroscopic redshift from [D. Kodra et al. \(2023\)](#) of $1.2 \leq z \leq 3.0$, which is similar to the range probed by A19. Finally, we limit our sample to faint sources with $S_{850\mu\text{m}} < 4 \text{ mJy}$.

There are twelve faint DSFGs that satisfy all of these criteria. In Table 1, we list the SUPER GOODS and CANDELS ID numbers of these faint DSFGs, their 850 μm fluxes, their CANDELS positions, the offsets between the SUPER GOODS and CANDELS positions, the F160W magnitudes, and the spectroscopic redshifts with references. We note that for GN-10283, we assume a spectroscopic redshift of $z = 1.224$ based on the detection of the [O II] $\lambda\lambda 3727, 3729$ doublet in its Keck/DEIMOS spectrum, rather than the $z = 1.219$ value given by [D. Kodra et al. \(2023\)](#) from earlier, less accurate Keck/LRIS spectra ([S. C. Chapman et al. 2005](#)).

Table 1. NIR Color-Selected Faint DSFGs

SUPER GOODS			CANDELS						
ID	$S_{850\mu\text{m}}$ (mJy)	ID	R.A.	Decl.	Offset ('')	F160W (AB mag)	z_{spec}	z_{ref}	AGN?
(1)	(2)	(3)	(4)	(5)	(6)	(7)	(8)	(9)	(10)
<i>NOEMA Targets</i>									
183	1.4 ± 0.3	13722	12:36:57.378	62:14:07.99	1.35	21.8	1.4599	a	No
149	2.1 ± 0.5	10601	12:37:41.381	62:12:51.22	2.18	20.7	1.6017	a	Yes
131	2.3 ± 0.4	3987	12:36:19.115	62:10:04.32	2.82	23.6	2.21 ± 0.03	f	No
110	2.9 ± 0.3	10283	12:36:34.523	62:12:40.99	1.15	20.8	1.224	c	Yes
90	3.5 ± 0.4	3835	12:36:31.281	62:09:58.00	1.02	23.0	2.2996	a,b	Yes
164	1.8 ± 0.4	23490	12:36:49.094	62:18:14.00	1.78	22.4	2.3197	a	No
175	1.6 ± 0.4	7630	12:37:13.195	62:11:45.55	2.05	24.3	2.4139	a	No
128	2.4 ± 0.4	19876	12:36:22.653	62:16:29.78	3.26	22.7	2.466	d,e	Yes
<i>Other Faint DSFGs (not observed)</i>									
143	2.1 ± 0.5	4295*	12:36:11.507	62:10:33.72	1.12	22.6	2.245	b	No
162	1.8 ± 0.5	7912#	12:36:08.824	62:11:43.78	2.77	20.7	1.336	g	No
152	2.0 ± 0.5	9568	12:36:49.875	62:12:33.52	4.69	22.9	2.487	b	No
118	2.7 ± 0.4	17815†	12:37:13.668	62:15:45.29	2.85	23.4	2.3008	a	No
<i>Serendipitously Detected DSFG</i>									
102	3.2 ± 0.4	8051	12:37:14.051	62:11:56.78	0.78	25.4	2.593	h	No

COLUMNS (1)–(2) are from L. L. Cowie et al. (2017)’s Table 4, while (3)–(6) are from G. Barro et al. (2019)’s Table 4. The columns are as follows: (1) SCUBA-2 850 μm source number; (2) 850 μm flux density; (3) CANDELS ID number; (4)–(5) CANDELS position from HST imaging; (6) offset between the SCUBA-2 and CANDELS positions; (7) HST/WFC3 F160W magnitude; (8) spectroscopic redshift; (9) reference for redshift, where a = M. Kriek et al. (2015), b = G. D. Wirth et al. (2015), c = our Keck/DEMOS [O II] $\lambda\lambda 3727, 3729$ redshift, d = S. C. Chapman et al. (2005), e = A. M. Swinbank et al. (2004), f = A. Pope et al. (2008), g = A. J. Barger et al. (2008), and h = D. J. Eisenstein et al. (2023); (10) whether the galaxy is associated with a Chandra X-ray source in Y. Q. Xue et al. (2016)’s point source catalog (i.e., all galaxies marked “Yes” are associated with a moderate luminosity AGN).

*Observed by the PdBI High- z Blue Sequence Survey-2 (PHIBSS-2; R. Genzel et al. 2015).

#Protected source under the ongoing NOEMA3D large program.

†Observed under NOEMA Project S21CV (P.I. L. Bing; S. Berta et al. 2025).

Four of the faint DSFGs are also associated with Chandra X-ray point sources, which are consistent with being AGNs with 2–7 keV luminosities $L_X < 5 \times 10^{43} \text{ erg s}^{-1}$ (Y. Q. Xue et al. 2016).

Four of the twelve faint DSFGs were not included in our final NOEMA sample: three are part of past or ongoing NOEMA programs (see the notes for Table 1), and the last, GN-9568, would have been the most expensive to observe in our sample due to its high redshift and low $S_{850\mu\text{m}}$. This left us with a final sample of eight NOEMA targets with $z = 1.224 - 2.466$, which we show in Figure 1 as the filled green stars. We show three-color cutouts of our eight NOEMA targets from the CANDELS HST imaging in Figure 2. Each cutout is centered on the 850 μm position and shows our 5'' radius for counterpart matching as a green circle. We also plot contours showing the IRAC2 emission in the same region. We mark the red-selected CANDELS galaxies with a red square, showing that each SCUBA-2 source has exactly one such counterpart.

2.5. Observing Strategy

We estimated the expected fluxes of CO transitions in NOEMA bands 1 (3 mm) or 2 (2 mm) at our targets’ redshifts by first generating a C. M. Casey (2012) modified blackbody + MIR power law spectral energy distribution (SED) for each galaxy with fiducial values of $\alpha = 2.0$, $\beta = 1.8$, and $T = 40$ K, normalized to the 850 μm flux. We integrated these SEDs to obtain FIR luminosities, $L_{\text{FIR}}^{40-400\mu\text{m}}$, and used the empirical $L'_{\text{CO}(4-3)} - L_{\text{FIR}}$ relations from D. Liu et al. (2015) to estimate the CO(4–3) fluxes. We then scaled the CO(4–3) values to CO(3–2) and CO(2–1) using the median CO spectral line energy distribution (SLED) from B21. We found that despite the higher noise in the 2 mm band, the brighter CO fluxes of higher- J emission lines gave us comparable observing time requirements for either 2 mm or 3 mm observations. We observed our targets at 2 mm to maximize the likelihood of obtaining continuum detections, which are helpful for constraining the dust emissivities of these faint DSFGs (see Section 5.2.3). We therefore targeted two different CO transitions, depending on the redshift of the target galaxy:

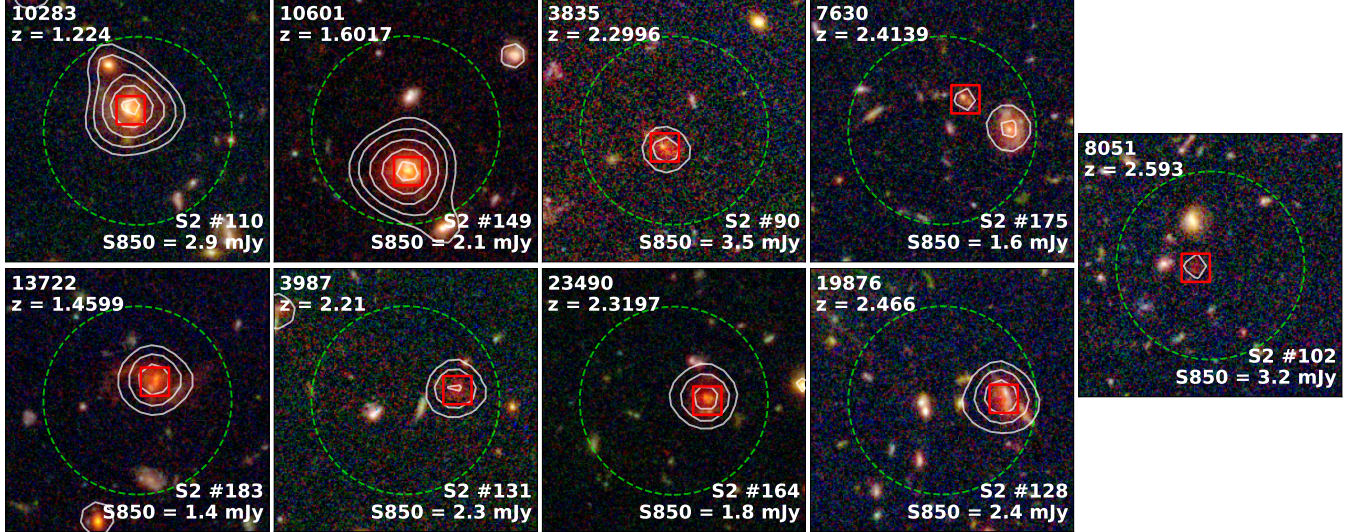


Figure 2. HST three-color thumbnails of our 8 original targets and the serendipitous NOEMA detection GN-8051 (rightmost panel; see Section 4.1). All cutouts use the HST filters $rgb = F160W/F814W/F435W$, with a contour of the Spitzer/IRAC 4.5 μm emission overlaid in white. Each cutout is 15'' on a side, centered on the SCUBA-2 position, and the green dashed circle of radius 5'' is the region within which we search for OIR counterparts. The red square in each thumbnail shows the sole red-selected (Equation 1) CANDELS galaxy within this region. The SCUBA-2 ID and 850 μm flux (L. L. Cowie et al. 2017) are shown in the bottom right corner of each thumbnail, while the CANDELS ID number (G. Barro et al. 2019) and spectroscopic redshift (D. Kodra et al. 2023) are shown in the top left corner.

- CO(3–2) ($\nu_{\text{rest}} = 345.786$ GHz) at $z < 2$, and
- CO(4–3) ($\nu_{\text{rest}} = 461.041$ GHz) at $z > 2$.

In two of the $z > 2$ galaxies, GN-3987 and GN-23490, we targeted both the CO(4–3) transition in the lower sideband (LSB) and the [C I] (${}^3\text{P}_1 - {}^3\text{P}_0$) transition ($\nu_{\text{rest}} = 492.161$ GHz; hereafter “[C I](1–0)”) in the upper sideband (USB). This gives all of our targeted lines expected sky frequencies of $\nu_{\text{exp}} = \nu_{\text{rest,CO}} / (1 + z_{\text{spec}}) = 133.00 - 155.83$ GHz. We list the expected frequency for each line in Table 2.

Two of our targets had previously been observed in CO surveys using the Plateau de Bure Interferometer (PdBI) and are reported in the compilation of M. S. Bothwell et al. (2013). These are GN-3987 (SMM 123618+621007), which has a “candidate”—rather than secure—CO(3–2) detection, due to its relatively weak (4.0σ) signal at $z_{\text{CO}} = 2.203$ and spatial offset from the SCUBA 850 μm position (M. S. Bothwell et al. 2013). In this work, we target its CO(4–3) line to confirm its redshift. Second, GN-10283 (SMM 123634+621241) is a $z = 1.22$ major merger with CO(2–1) (D. T. Frayer et al. 2008), CO(4–3) (M. S. Bothwell et al. 2013), and CO(6–5) (H. Engel et al. 2010) detections, but not CO(3–2), which we observe in this work. Integration on GN-10283 constituted $\approx 4\%$ of our usable on-source time.

Our NOEMA observations were conducted between December 2023 and November 2024 in the compact C and D configurations, under NOEMA Projects W23CH (P.I. M. Nicandro Rosenthal) and S24BR (P.I. M. Nicandro Rosenthal). Our observations consisted of nine tracks, totaling 29.5 hr of observing time, with our targets distributed among

five observing setups with local oscillator (LO) frequencies $\nu_{\text{LO}} = 139 - 149$ GHz. In Column (2) of Table 2, we list the setup that we used for each source; sources in the same setup were observed in track-sharing mode to minimize calibration overheads.

3. REDUCTION AND ANALYSIS

We reduced all of our NOEMA data using the standard calibration pipeline in the Continuum and Line Interferometry Calibration (CLIC) component of GILDAS, the IRAM data reduction and analysis software suite. The calibrators used varied by track among the following sources: 1125+596, 1214+588, and J1302+690 were used for gain calibration; 0923+392, 3C84, and 3C454.3 for bandpass calibration; and MWC 349 and LKH α 101 for absolute flux calibration. We performed additional manual flagging of both usable tracks in setup s24br003, which had degrading weather conditions at the end of each track that prevented good amplitude and phase versus time fits. For all other tracks, we used the default pipeline output on all of the available data.

Following calibration, we used the CLIC data quality assessment (DQA) tool to flag scans within the calibrated data that have high phase rms noise or large amplitude losses, using the default detection experiment settings. Our final calibrated uv data tables were generated from the remaining data. In Column (8) of Table 2, we give the total usable integration time on each source after running the DQA. These range between 0.5 hr for the brightest source (GN-10283) and 4.2 hr for the faintest source (GN-7630). In total, our survey obtained 13.6 hr of usable on-source integration time.

Table 2. NOEMA Spectral Line Observations

ID	Setup	Config.	Line	ν_{exp} (GHz)	SB	Beam ($'' \times ''$, deg.)	t_{int} (hr)	rms_{ch} (mJy beam $^{-1}$)
(1)	(2)	(3)	(4)	(5)	(6)	(7)	(8)	(9)
3987	w23ch001	12C	CO(4–3)	143.63	L	1.55 \times 1.26, -12.2	2.1	0.41
			[C I](1–0)	153.32	U	1.40 \times 1.13, -13.9	2.1	0.51
13722	w23ch001	12C	CO(3–2)	140.57	L	1.55 \times 1.25, -9.3	2.1	0.40
10601	w23ch002	12C	CO(3–2)	133.00	L	1.79 \times 1.10, 13.9	2.2	0.43
3835	s24br001	10D	CO(4–3)	139.63	L	4.01 \times 2.58, -55.1	1.2	0.91
10283	s24br001	10D	CO(3–2)	155.83	U	3.61 \times 2.33, -54.9	0.5	1.73
7630	s24br002	10D	CO(4–3)	135.04	L	3.60 \times 2.43, -59.4	4.2	0.34
8051*	s24br002	10D	[C I](1–0)	136.98	L	3.60 \times 2.43, -59.4	4.2	0.53*
19876	s24br003	C/D**	CO(4–3)	133.02	L	2.83 \times 2.24, 63.0	0.6	0.88
23490	s24br003	C/D**	CO(4–3)	138.88	L	2.82 \times 2.25, 64.2	0.7	0.81
			[C I](1–0)	148.25	U	2.49 \times 2.06, 70.7	0.7	0.98

*GN-8051 was a serendipitous detection in the same pointing as GN-7630, located 12.315 $''$ from the pointing center. The quoted value of $\sigma_{20\text{MHz}}$ includes a mean primary beam correction factor across the LSB of this tuning of 1.54.

**Setup s24br003 includes one track taken on 05-Oct-2024 in the 10D configuration, and one track taken on 04-nov-2024 in the 12C–N020+N017 configuration.

3.1. Imaging

We generated first-look dirty image cubes of each sideband with a targeted emission line in MAPPING, the imaging and deconvolution suite of GILDAS. We first resampled the spectral axis of each data cube by a factor of 10, which yielded channel widths of 20 MHz ($\Delta v \approx 40 \text{ km s}^{-1}$ at $\nu_{\text{obs}} \approx 150 \text{ GHz}$). We removed the first and last 10 channels and the central 2 channels, which are susceptible to noise spikes, from the resampled cubes, and imaged these with natural weighting and fixed pixel sizes of 0.25 $'' \times 0.25''$. Each image cube was generated with 256 \times 256 pixels, or 64 $'' \times 64''$, ensuring that the imaged region extends up to at least the FWHM of the NOEMA primary beam ($\theta_{\text{HPBW}} = 32''$ at 150 GHz).

The naturally weighted images have spatial resolutions of roughly 1.5 $'' \times 1.2''$ for observations in the 12C configuration and 3.6 $'' \times 2.4''$ for observations in the 10D configuration. In Table 2, we give the specific values for each sideband with a targeted emission line. These are sufficiently coarse that we expect all of our targets to be unresolved, given the typical size of dust and gas emission from DSFGs (e.g., [J. A. Hodge et al. 2016](#)).

For all images and/or image cubes, we measured the rms in the image plane by masking out a circular region centered on the CANDELS position, with a radius equal to three times the synthesized beam FWHM, and then taking the rms of the flux in 1000 randomly drawn pixels in a circular region extending one primary beam FWHM from the phase center. We refer to these noise values measured in the image plane as $\text{rms}_{2\text{D}}$ throughout the remainder of this work. In cases where an off-axis source was detected in the image (see Section 4.1),

we also masked out a circular region of the same size around that source's position.

3.2. 1D Spectra

To generate a 1D spectrum for each line in Table 2, we started by summing all channels within $\pm 2000 \text{ km s}^{-1}$ of the expected frequency of the line, and we identified the brightest spaxel in this image within one synthesized beam FWHM of the CANDELS position. We then extracted a 1D spectrum from this spaxel. We measured the spectral noise on a channel-by-channel basis using the procedure described in Section 3.1.

To correct for the lower primary beam response at positions offset from the phase center of each NOEMA pointing, we approximated the response of the NOEMA primary beam as an Airy function. We performed all of our flux and noise measurements on the uncorrected images or visibilities, and we multiplied the rms and flux values by our primary beam correction afterward, in order to preserve signal-to-noise (S/N).

3.3. Emission Line Fitting

3.3.1. 1D Fits

To identify emission lines in our data, we performed a two-step Gaussian fitting procedure on the primary beam-corrected 1D spectrum for each line in Table 2, using a simple least-squares fitter. The first Gaussian fit was used to approximate the mean frequency, $\bar{\nu}$, and Gaussian width, σ , of the emission line. We then fit a first-order baseline to the channels at least $\pm 2\sigma$ from the mean of this Gaussian and subtracted this baseline. Finally, we re-fit the baseline-subtracted spectrum to obtain final values of $\bar{\nu}$, σ , and S_{peak} .

We measured uncertainties in these parameters by conducting Monte Carlo (MC) simulations of the above fitting procedure with noise-injected synthetic spectra. For each real 1D spectrum, we represented each channel as a Gaussian distribution with a mean equal to the flux in that channel and standard deviation equal to the rms in that channel. We then drew 10 000 random values from these distributions, resulting in 10 000 synthetic spectra, which we fit using the same two-step procedure above.

Following M. S. Bothwell et al. (2013) and B21, we consider channels with frequencies between $\bar{\nu} \pm 2\sigma$ to be those containing line emission. We estimated the 1D S/N of the fit lines to be

$$S/N_{1D} = \sqrt{N_{\text{ch}}} \cdot \frac{\langle S \rangle}{\langle \text{rms}_{\text{ch}} \rangle}, \quad (2)$$

where $\langle S \rangle$ and $\langle \text{rms}_{\text{ch}} \rangle$ are the average flux and rms, respectively, across all line channels. We classified the fit emission lines as secure detections if $S/N_{1D} \geq 5$, and as tentative detections if $3 \leq S/N_{1D} < 5$.

3.3.2. Line-Only Fluxes and Images

Following our 1D fits, we fit a 1st-order baseline to the line-free channels in the calibrated visibilities for each detected line, subtracted this baseline from the *uv* data, and then averaged these continuum-subtracted data to produce a single-channel line-only *uv* dataset. We imaged these data using the settings described in Section 3.1, and we measured the uncorrected rms noise in these images following the procedure in Section 3.1.

We measured the positions and fluxes of the secure and tentative line detections by directly fitting the line-only *uv* data using the `uv_fit` task, with initial guesses for the fit allowed to vary by $\pm 2''$ from the CANDELS position. We then converted these into integrated flux units by multiplying in the bandwidth used to generate the line-only maps:

$$I_{\text{line}} = \langle S_{\text{line}} \rangle_{2D} \cdot 4\sigma, \quad (3)$$

where $\langle S_{\text{line}} \rangle_{2D}$ is the best-fit flux density from `uv_fit`, and σ is the Gaussian width from our 1D fits.

For lines detected with $S/N_{2D} > 5$, we deconvolved the images using a J. A. Högbom (1974) CLEAN with a gain of 0.1, limited to an elliptical region twice the size of the synthesized beam FWHM centered on the line position from `uv_fit`. We stopped each CLEAN when the maximum value in the residual image in this region reached $2 \times \text{rms}_{2D}$. We recalculated the rms noise on the cleaned images, and we calculated the S/N of the lines in the image plane as

$$S/N_{2D} = \frac{\langle S_{\text{line}} \rangle_{2D}}{\text{rms}_{2D}}. \quad (4)$$

We describe the results of this analysis in Section 4.2.

4. RESULTS

4.1. Serendipitous DSFG Detections

Visual inspection of our NOEMA images revealed additional sources within the NOEMA primary beam in two of our pointings (see Figure 3). Each of these additional sources is coincident with an SMA position from L. L. Cowie et al. (2017), indicating they are real DSFGs. The two galaxies are

GN-8051—This galaxy was detected at R.A. = 12:37:14, Dec. = +62:11:56.8, offset by 12.7'' from the pointing center targeting GN-7630. This position is coincident with both the CANDELS galaxy GN-8051 (G. Barro et al. 2019) and the SMA position of 850 μm source #102 ($S_{850\mu\text{m}} = 3.2 \pm 0.38 \text{ mJy}$) in L. L. Cowie et al. (2017). The CANDELS counterpart satisfies our red selection (Equation 1; see cyan diamond in Figure 1). GN-8051 was also observed with NIRSpec as part of the JWST Advanced Deep Extragalactic Survey (JADES; D. J. Eisenstein et al. 2023, ID = 77760) and found to have $z_{\text{spec}} = 2.593$. There are no CO lines at this redshift in our spectral coverage of GN-8051, but the LSB does cover the [C I](1–0) line at $\nu_{\text{exp}} = 136.98 \text{ GHz}$. Because it satisfies our selection criteria, we fit the [C I] and 2 mm continuum emission of GN-8051 using the procedure outlined in Section 3.3. We list the source's properties at the bottom of Table 1, and we include its thumbnail as the right-most panel of Figure 2.

GN-19084—We identified another source at R.A. = 12:36:22.1, Dec. = +62:16:16, offset by 14.6'' from the pointing center targeting GN-19876. This position is consistent with the CANDELS galaxy GN-19084 (G. Barro et al. 2019) and with the SMA position of source #42 ($S_{850\mu\text{m}} = 5.4 \pm 0.41$) in L. L. Cowie et al. (2017). It does not have a spectroscopic redshift from G. Barro et al. (2019) or in JADES, and we do not identify any emission lines in this source. We measure and report its 2 mm continuum flux in Section 4.3.

4.2. Emission Line Detections

We obtained secure detections of 7/8 of our targeted CO lines (see Columns (2) and (3) of Table 3), as well as a secure detection of [C I](1–0) in GN-3987 and a marginal [C I] detection in GN-8051. In Figure 4, we show the baseline-subtracted, primary beam-corrected spectra and their best-fit Gaussian profiles. Each panel shows a total bandwidth of 2500 km s^{-1} centered on the best-fit redshift. We highlight the line channels (those within $\pm 2\sigma$ of the best-fit redshift) in blue for CO and in orange for [C I]. Our CO detections have full widths at half-maximum (FWHM $\equiv 2.355\sigma$) in the range 263–963 km s^{-1} , slightly above the range of CO lines in the ASPECS-LP sample (FWHM = 40–609 km s^{-1} ; A19). In Columns (4) and (5) of Table 3, we list the best-fit redshifts and FWHM of the detected lines. The uncertainties

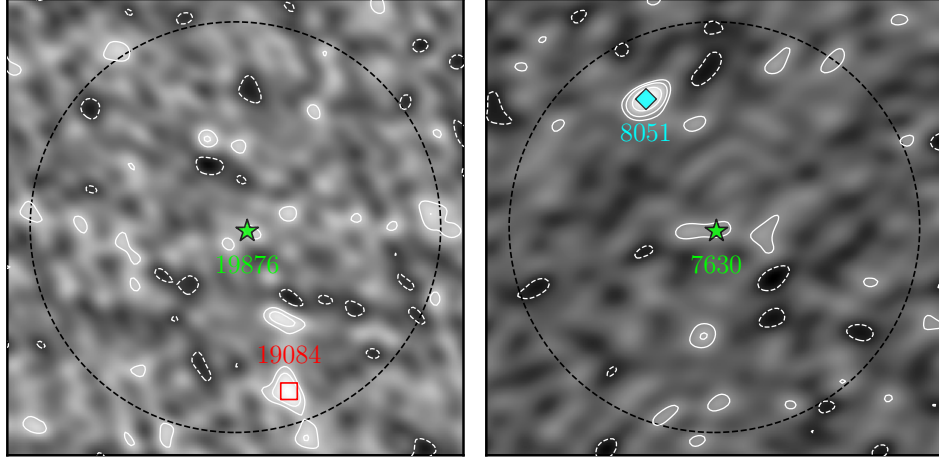


Figure 3. NOEMA 2 mm continuum images with serendipitous off-axis detections. In both cases, the main target that the pointing is centered on is marked by the green star, as in Figure 1, and the black dashed circle shows the extent of the primary beam. Contours are at $S/N = -2$ (dashed), 2, 3 and 5. *Left:* Continuum image of the USB, centered on the CANDELS position of GN-19876, with the off-axis source GN-19084 marked by a red square. *Right:* Same, but for the image centered on GN-7630, with GN-8051 marked by the cyan diamond, as in Figure 1.

Table 3. Emission Lines

ID	Line	S/N _{1D}	z	FWHM	I	L'	$L'_{\text{CO}(1-0)}$	M_{mol}
(1)	(2)	(3)	(4)	(km s ⁻¹)	(Jy km s ⁻¹)	(10 ¹⁰ K km s ⁻¹ pc ²)	(10 ¹⁰ K km s ⁻¹ pc ²)	(10 ¹⁰ M_{\odot})
10283	CO(3-2)	9.6	1.224	581 ⁺⁶⁰ ₋₇₆	3.29 ± 0.30	2.90 ± 0.26	4.60 ± 0.97	22.5 ± 4.7
13722	CO(3-2)	9.9	1.460	369 ⁺³⁴ ₋₃₇	0.64 ± 0.05	0.79 ± 0.06	1.25 ± 0.26	6.1 ± 1.3
10601	CO(3-2)	8.5	1.599	589 ⁺⁶⁶ ₋₆₅	0.71 ± 0.07	1.04 ± 0.11	1.65 ± 0.36	8.1 ± 1.8
3987	CO(4-3)	11.0	2.215	374 ± 35	0.72 ± 0.06	1.07 ± 0.08	3.14 ± 0.44	15.4 ± 2.2
	[C I](1-0)	5.5	2.215	306 ⁺⁵¹ ₋₇₃	0.39 ± 0.05	0.51 ± 0.07	2.30 ± 0.33	11.3 ± 1.6
3835	CO(4-3)	10.7	2.304	963 ⁺⁷³ ₋₇₈	3.13 ± 0.48	4.94 ± 0.76	14.54 ± 2.81	71.2 ± 13.8
23490	CO(4-3)	6.0	2.319	263 ⁺⁵² ₋₇₄	0.75 ± 0.09	1.19 ± 0.14	3.50 ± 0.57	17.1 ± 2.8
	[C I](1-0)	1.3*	2.319*	263*	< 0.24	< 0.36	< 1.62	< 7.9
7630	CO(4-3)	5.1	2.415	444 ⁺³⁶⁴ ₋₁₆₃	0.35 ± 0.05	0.59 ± 0.09	1.74 ± 0.34	8.5 ± 1.7
19876	CO(4-3)	1.1*	2.466*	409*	< 0.54	< 0.96	< 3.20	< 15.7
8051	[C I](1-0)	3.2	2.595	510 ⁺¹²⁰ ₋₂₁₂	0.35 ± 0.08	0.60 ± 0.14	2.70 ± 0.64	13.2 ± 3.1

COLUMNS: (1) CANDELS ID (G. Barro et al. 2019); (2) observed transition; (3) signal-to-noise of the line in the single-spaxel spectrum, given by Equation 2; (4) best-fit redshift; (5) best-fit FWHM with uncertainties from our MC simulations (see Section 3.3.1); (6) integrated line flux; (7) line luminosity; (8) luminosity of the fundamental CO(1-0) transition, converted using the average CO SLED from B21 for the CO lines and using the average [C I](1-0) to CO(1-0) ratio from Q. Jiao et al. (2017) for the [C I] lines (see Section 5.1 for details); (9) molecular gas mass, assuming $\alpha_{\text{CO}} = 3.6$.

*—For upper limits, Column (3) gives the 1D signal-to-noise of the best-fit Gaussian, but Columns (4) and (5) give the *fixed* redshift and FWHM used to generate the “line” images on which the upper limits in Columns (7)–(9) are measured.

on the FWHM are the 16th to 84th percentile values of the distributions of these parameters from our MC simulations.

The CO and [C I] redshifts from our NOEMA emission line detections are consistent with their existing OIR spectroscopic redshifts, which are shown by the vertical dashed lines in Figure 4. Alongside each spectrum, we also show the line-only image for the detected line (see Section 3.3.2), and mark the CANDELS position with the red circle and cross. All of our line detections are coincident with the red-selected CANDELS source position within $< 1''$.

Notably, in GN-3987, we detect both CO(4-3) and [C I](1-0) at $z = 2.215$, rather than the $z = 2.203$ of the “candidate” CO(3-2) line associated with its SCUBA-2 source (M. S. Bothwell et al. 2013). Both redshifts are consistent with the highly uncertain D. Kodra et al. (2023) redshift of $z = 2.21 \pm 0.03$, which was fit to broad polycyclic aromatic hydrocarbon features in the MIR spectrum (A. Pope et al. 2008). However whereas both of our line detections have positions coincident with the red CANDELS galaxy (and a F. Owen 2018 radio source), the candidate CO(3-2) detection

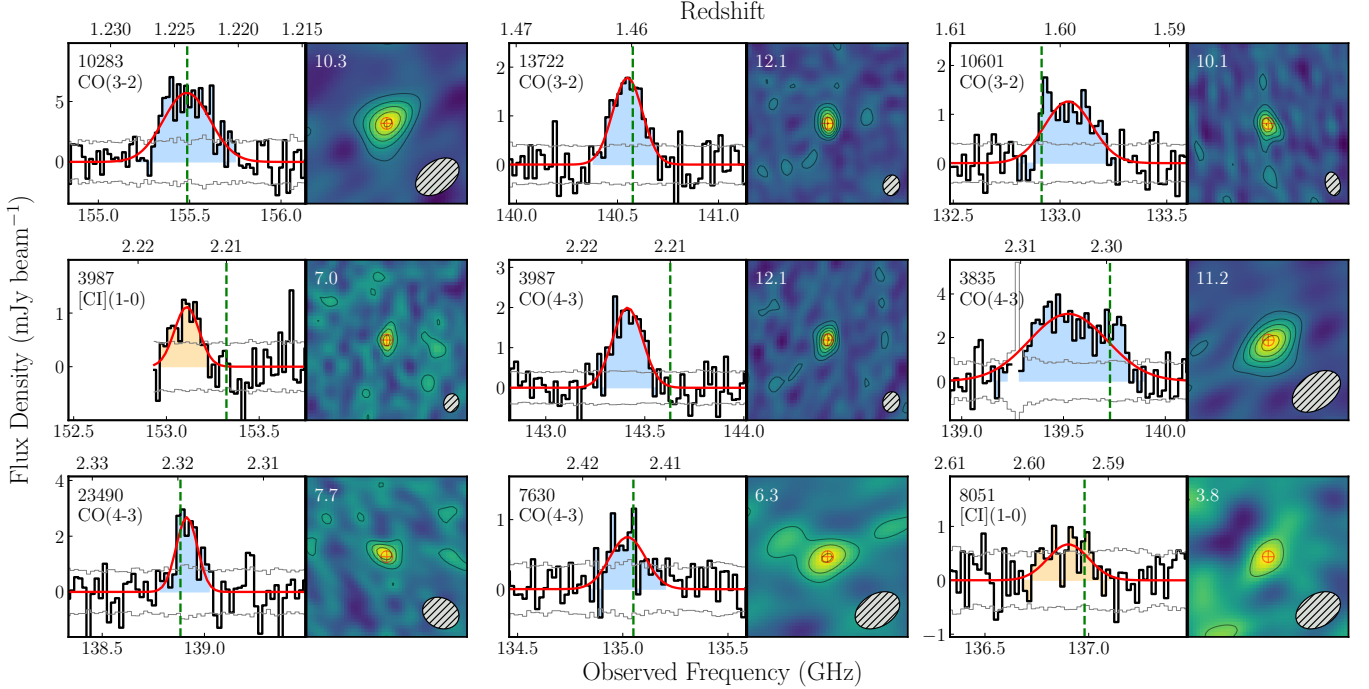


Figure 4. NOEMA spectra and images of the nine detected emission lines in our sample. In each spectrum, the CANDELS ID of the source and the targeted line are given in the top left corner, the black line is the continuum-subtracted and primary beam-corrected spectrum, the gray line is the rms noise per channel, the vertical dashed green line is the OIR spectroscopic redshift (see Table 1), and the red curve is the best-fitting Gaussian. Blue and orange shading show the line channels ($\pm 2\sigma$ from the center) for CO and [C I] emission, respectively. All spectra show a bandwidth of 2500 km s^{-1} centered on the Gaussian. To the right of each spectrum is a $12'' \times 12''$ thumbnail showing the cleaned line-only images produced from these channels, with the NOEMA synthesized beam shape shown in the bottom right corner. Each thumbnail is centered on the CANDELS position, which is shown by the red circle and cross. The 2D S/N of these images is given in the top left corner of each thumbnail. Contours are at 2, 4, 6, 8, 10, and 12σ .

was located $3.6''$ away. We extracted 1D spectra from our NOEMA data at the M. S. Bothwell et al. (2013) position to search for CO(4-3) and [C I](1-0) at $z = 2.203$, but find no evidence of either line, despite our deeper observations. We therefore adopt our new redshift of $z = 2.215$ for GN-3987 for the remainder of this work.

4.2.1. Integrated Fluxes and Luminosities

We measure integrated CO fluxes of $I_{\text{CO}} = 0.36 - 3.27 \text{ Jy km s}^{-1}$ in the detected emission lines, with five of our seven detections having $I_{\text{CO}} < 1 \text{ Jy km s}^{-1}$. We convert the integrated fluxes to line luminosities, in brightness temperature units, via Equation 3 from P. M. Solomon & P. A. Vanden Bout (2005):

$$L'_{\text{line}} [\text{K km s}^{-1} \text{ pc}^2] = \frac{3.25 \times 10^7 I_{\text{line}} D_{\text{L}}^2}{\bar{\nu}^2 (1+z)^3}, \quad (5)$$

where I_{line} is the integrated line flux in Jy km s^{-1} , $\bar{\nu}$ is the line sky frequency in GHz, and D_{L} is the luminosity distance in Mpc, calculated using the redshift of the CO or [C I] line. We obtain line luminosities of $L'_{\text{line}} = (0.5 - 4.9) \times 10^{10} \text{ K km s}^{-1} \text{ pc}^2$, or $L'_{\text{line}} = (0.6 - 4.9) \times 10^{10} \text{ K km s}^{-1} \text{ pc}^2$ for just the CO detections. In Columns

(6) and (7) of Table 3, we give the integrated fluxes and line luminosities for each emission line.

To measure upper limits to the integrated fluxes of the two undetected lines—CO(4-3) in GN-19876 and [C I] in GN-23490—we generated continuum-subtracted, line-only datasets for these sources assuming a fixed redshift and FWHM, rather than using the low-S/N Gaussian fits. For the [C I](1-0) line in GN-23490, we used the redshift and FWHM of the detected CO(4-3) line ($z = 2.319$ and FWHM = 263 km s^{-1}). For GN-19876, since there is no other line to reference for FWHM, we assumed the OIR redshift of $z = 2.466$ and FWHM = 409 km s^{-1} , which is the median FWHM of the detected CO(4-3) lines in our sample. We then imaged these and measured the rms in the image plane in the same way that we did for the detected emission lines. We took the upper limits to the integrated fluxes to be

$$I_{\text{line}} \leq 4 \cdot \text{rms} \cdot 4\sigma. \quad (6)$$

Here, σ is the assumed Gaussian line width.

In Table 3, we provide the upper limits to the integrated fluxes and corresponding line luminosities for the two undetected lines. We note that in addition to the errors listed in this

Table 4. NOEMA Continuum Fluxes and Upper Limits

ID	ν (GHz)	LSB		USB	
		Flux ($\mu\text{Jy beam}^{-1}$)	ν (GHz)	Flux ($\mu\text{Jy beam}^{-1}$)	ν (GHz)
<i>Detections</i>					
3835	139.3	197 \pm 41	154.7	255 \pm 70	
3987	141.3	94 \pm 18	156.7	177 \pm 22	
8051	136.3	173 \pm 25	151.7	261 \pm 33	
19084	—	—	151.7	539 \pm 99	
<i>Non-detections</i>					
19084	136.3	< 336	—	—	
7630	136.3	< 69	151.7	< 72	
10283	139.3	< 281	154.7	< 286	
10601	131.3	< 74	146.7	< 84	
13722	141.3	< 52	156.7	< 62	
19876	136.3	< 175	151.7	< 166	
23490	136.3	< 148	151.7	< 149	

Table, all of our NOEMA measurements are subject to systematic uncertainties in absolute flux calibration of $\sim 10\%$.

4.3. 2 mm Continuum

Following the identification of emission lines in our NOEMA images, we generated continuum-only uv data and images for each sideband by averaging together all of the line-free channels (i.e., those falling outside of $\pm 2\sigma$ from the best-fit line center). We then measured the fluxes and positions of continuum emission in the uv plane, as well as imaging and deconvolving the continuum data, using the same procedure we used to measure and image our line-only images (Section 3.3.2). For sidebands with off-axis sources (see Section 4.1), we fit point sources to both positions simultaneously, giving `uv_fit` initial guesses for the source position within $\pm 2''$ of each CANDELS position.

We classified a continuum source as a detection if the best-fit point source flux exceeded both 4 times the rms in that image and the absolute value of the most negative pixel value within the extent of the NOEMA primary beam. The S/N of these negative “sources” ranged from -2.6 to -4.4 , with stronger negative peaks in the C and C/D configuration images, as expected given the higher number of independent synthesized beams that cover the primary beam area at higher spatial resolution.

Using these criteria, we detected continuum emission in both sidebands in GN-3835, GN-3987, and GN-8051, as well as in the USB of GN-19084. We report these values, along with the central frequency of the sideband in which they were measured, in Table 4. For all of the sidebands without continuum detections, we provide upper limits (either $4 \times \text{rms}_{2\text{D}}$ or the inverse of the most negative peak, whichever is greater) in Table 4.

5. PHYSICAL PROPERTIES

5.1. Molecular Gas Masses from CO Line Luminosities

We derived molecular gas mass estimates for the eight galaxies in our NOEMA sample—the seven CO detections and the CO(4–3) upper limit for GN-19876—from their CO line luminosities. We first converted the luminosities of the observed CO transitions to those of the fundamental CO(1–0) transitions by assuming the median values of $r_{31} \equiv L'_{\text{CO}(3-2)}/L'_{\text{CO}(1-0)} = 0.63 \pm 0.12$ and $r_{41} \equiv L'_{\text{CO}(4-3)}/L'_{\text{CO}(1-0)} = 0.34 \pm 0.04$ from B21. We give these CO(1–0) luminosities in Column (8) of Table 3. We note that the line ratios for individual DSFGs can vary significantly—for example, D. A. Riechers et al. (2020) measured $r_{31} = 0.23 - 1.56$ in a sample of six ASPECS galaxies with follow-up CO(1–0) detections using the VLA; and A19 used ratios of $r_{31} = 0.42 \pm 0.07$ and $r_{41} = 0.31 \pm 0.06$, which were derived from a survey of BzK -selected massive main sequence galaxies at $z = 1.5$ (E. Daddi et al. 2015).

The galaxies’ CO(1–0) luminosities are then related to the molecular gas by

$$M_{\text{mol}} = 1.36 \alpha_{\text{CO}} L'_{\text{CO}(1-0)}, \quad (7)$$

where the factor of 1.36 accounts for a 10% Helium fraction, and the conversion factor α_{CO} has units of $M_{\odot} (\text{K km s}^{-1} \text{ pc}^2)^{-1}$. The CO conversion factor varies based on several factors, especially metallicity (see, e.g., the review by A. D. Bolatto et al. 2013). In this work, we assume a fiducial value of $\alpha_{\text{CO}} = 3.6$ (E. Daddi et al. 2010), which is consistent with the analysis of ASPECS-LP (A19), though we note that other studies have adopted lower values (e.g., $\alpha_{\text{CO}} = 1.0$, M. S. Bothwell et al. 2013).

Our measured gas masses using Equation 7 are in the range $\log M_{\text{mol}}/M_{\odot} = 10.8 - 11.9$ dex, with a median of 11.2 dex. From the CO(4–3) upper limit in GN-19876, we inferred an upper limit of $\log M_{\text{mol}}/M_{\odot} < 11.2$ dex. In Column (9) of Table 3, we list the gas mass or upper limit that we derived from each targeted CO line.

5.1.1. Neutral Carbon-based Gas Masses

Molecular gas can also be inferred from the [C I](1–0) line, and we measure [C I]-based gas masses for the three galaxies with spectral coverage of this line. We assume a line luminosity (or conversion factor) ratio of $L'_{\text{CO}(1-0)}/L'_{\text{[CI]}(1-0)} = \alpha_{\text{[CI]}}/\alpha_{\text{CO}} = 4.5 \pm 0.2$, which is the median value for local ULIRGs (Q. Jiao et al. 2017) and similar to $\alpha_{\text{[CI]}}/\alpha_{\text{CO}} \sim 4.5$ found for $z > 2$ DSFGs (e.g., B21; L. Dunne et al. 2022). In Columns (8) and (9) of Table 3, we give these CO(1–0) luminosities or upper limits, and the gas masses derived from them.

The two galaxies with both CO(4–3) and [C I](1–0) in our spectral coverage are GN-23490 and GN-3987. GN-3987 has

strong detections of both lines. We inferred gas masses of 1.5×10^{11} and $1.1 \times 10^{11} M_{\odot}$ from CO(4–3) and [C I](1–0), respectively, which are nearly in agreement. We do not detect the [C I](1–0) line in GN-23490, and the gas mass inferred from the CO(4–3) detection is 2.3 times higher than the 4σ upper limit on the [C I]-derived mass. High CO(4–3) to [C I](1–0) ratios can indicate higher gas densities, which allow the CO to be shielded against photodissociation by the interstellar radiation field (M. J. Kaufman et al. 1999). We note that GN-23490 has the lowest FWHM of any CO detection in our sample, which may support a dense, central gas reservoir scenario.

For the purposes of calculating derived properties that depend on M_{mol} (Section 6), we exclusively use the CO-based M_{mol} measurements where available, since there are many more CO-based gas masses in the literature than [C I]-based masses. This allows us to minimize systematic uncertainties when comparing the gas properties of our sample to those of other CO surveys and discussing strategies for future surveys of the faint DSFG population.

5.2. SED Fitting

To estimate the physical properties of the DSFGs that host the molecular gas reservoirs that we measured in Section 5.1, we fit the DSFGs’ SEDs using two different fitting codes. To measure the dust attenuation and stellar masses, we used BAGPIPES (Bayesian Analysis of Galaxies for Physical Inference and Parameter EStimation; A. C. Carnall et al. 2018), a stellar population synthesis (SPS)-based code, on the full UV-to-mm photometry of our sample. Second, we performed FIR-only modified blackbody (MBB) fits (S. J. McKay et al. 2023) to obtain SFH-independent measurements of our galaxies’ SFRs. We describe the input photometry, our fitting procedure, and the resulting estimated physical properties in the remainder of this Section.

5.2.1. Input Photometry

We performed our SED fits using the CANDELS UV-to-NIR photometry from G. Barro et al. (2019), supplemented with longer wavelength data from the literature. The CANDELS photometry includes ground-based U , K , and K_s imaging, five HST/ACS and four WFC3-IR bands, and all four Spitzer/IRAC bands. At longer wavelengths, we used Spitzer/MIPS 24 μm , Herschel/PACS 100 and 160 μm , and Herschel/SPIRE 250 and 350 μm fluxes from the GOODS-Herschel survey (D. Elbaz et al. 2011), with all nine faint DSFGs in this work having a match with an angular separation of $< 1''$; 450 and 850 μm SCUBA-2 fluxes from SUPER GOODS; 1.3 mm fluxes or upper limits from the NIKA-2 Cosmological Legacy Survey (L. Bing et al. 2023); and our NOEMA 2 mm fluxes and upper limits from Table 4. If a source was not found in any of the above catalogs, then we

measured an upper limit by taking the noise value at the position of the CANDELS galaxy.

5.2.2. BAGPIPES: A_V , Stellar Mass, L_{IR} , and SFR

We ran our BAGPIPES UV-to-mm fits using the stellar population models of G. Bruzual & S. Charlot (2003) and a physically motivated silicate–graphite–PAH dust emission model from B. T. Draine & A. Li (2007). We assumed a delayed SFH with an optional starburst, with logarithmic priors on the age and decay time, τ , of both SFH components, an ionization parameter of $\log U$ between -3.5 and -2 , and a wide range of PAH emission fractions and metallicities. We assumed a S. Charlot & S. M. Fall (2000) dust attenuation curve. These models and parameters were selected to resemble those of the Multi-wavelength Analysis of Galaxy PHYSical properties (MAGPHYS; E. da Cunha et al. 2008) code, which was used to measure the properties of the CO-detected DSFGs in A19 and B21. In Figure 5, we show the resulting SEDs for each galaxy, and in Table 5, we give the medians and 68% CL errors on A_V , $\log M_{\star}/M_{\odot}$, and $\log L_{\text{IR}}/L_{\odot}$ from our fits.

In Table 5, we also provide two different measures of the SFR. SFR_{SED} is the 100 Myr average of the fitted SFH in BAGPIPES, and SFR_{KE12} is calculated from L_{IR} using the relation:

$$\text{SFR}_{\text{KE12}} [M_{\odot} \text{ yr}^{-1}] = 1.41 \times 10^{-10} L_{\text{IR}} [L_{\odot}], \quad (8)$$

from R. C. Kennicutt & N. J. Evans (2012, hereafter KE12), which is scaled to a G. Chabrier (2003) initial mass function (IMF). The latter measurement is also sensitive to star formation over ~ 100 Myr timescales.

Our sample has $\text{SFR}_{\text{KE12}} = 140 - 690 M_{\odot} \text{ yr}^{-1}$, with a median of $370 M_{\odot} \text{ yr}^{-1}$. For all nine of our galaxies, these are higher than the SFRs returned by BAGPIPES, which span a range of $\text{SFR}_{\text{SED}} = 60 - 180 M_{\odot} \text{ yr}^{-1}$, with a median SFR_{SED} of $135 M_{\odot} \text{ yr}^{-1}$. The median ratio of these two SFR measures in our sample is $\langle \text{SFR}_{\text{KE12}}/\text{SFR}_{\text{SED}} \rangle = 2.1$ (0.32 dex), and the largest individual ratio is a factor of 10, in GN-3835. This median offset is large, but it is consistent with uncertainties in SFRs generated by SPS-based SED fitting codes (~ 0.1 – 0.5 dex; C. Pacifici et al. 2015). The individual offsets are also consistent with findings that SED fits that use parametric SFHs (such as MAGPHYS and our BAGPIPES fits) can underpredict SFRs for individual galaxies by up to an order of magnitude (A. C. Carnall et al. 2019) compared to the KE12 relations.

For the remainder of this work, we use SFR_{KE12} unless otherwise stated, since this minimizes differences between measured SFRs due to SED fitting assumptions, and it allows us to compare easily the properties of our faint DSFG sample to those of other samples, as most authors provide L_{IR} .

We caution that for the serendipitously-detected GN-8051, which is the OIR-faintest (F160W = 25.4 mag) and red-

Table 5. Physical Properties

ID	A_V (mag)	$\log \frac{M_\star}{M_\odot}$	SFR _{SED} ($M_\odot \text{ yr}^{-1}$)	$\log \frac{L_{\text{IR}}}{L_\odot}$	SFR _{KE12} ($M_\odot \text{ yr}^{-1}$)	ΔMS (dex)	$\log \frac{M_{\text{mol}}}{M_\odot}$	t_{dep} (Gyr)	μ_{mol}
(1)	(2)	(3)	(4)	(5)	(6)	(7)	(8)	(9)	(10)
10283	$1.69^{+0.04}_{-0.04}$	$11.12^{+0.01}_{-0.02}$	155^{+21}_{-19}	$12.56^{+0.02}_{-0.02}$	517^{+21}_{-20}	$0.78^{+0.02}_{-0.04}$	$11.35^{+0.08}_{-0.10}$	0.44 ± 0.09	1.70 ± 0.35
13722	$1.89^{+0.04}_{-0.04}$	$11.06^{+0.03}_{-0.03}$	87^{+5}_{-6}	$12.00^{+0.04}_{-0.04}$	142^{+12}_{-12}	$0.15^{+0.04}_{-0.06}$	$10.79^{+0.08}_{-0.10}$	0.43 ± 0.09	0.53 ± 0.11
10601	$1.38^{+0.09}_{-0.09}$	$11.52^{+0.02}_{-0.02}$	98^{+64}_{-31}	$12.43^{+0.03}_{-0.03}$	382^{+23}_{-22}	$0.17^{+0.03}_{-0.05}$	$10.91^{+0.09}_{-0.11}$	0.21 ± 0.05	0.24 ± 0.05
3987	$2.85^{+0.12}_{-0.10}$	$11.47^{+0.05}_{-0.04}$	136^{+15}_{-14}	$12.26^{+0.05}_{-0.05}$	256^{+28}_{-28}	$-0.16^{+0.05}_{-0.08}$	$11.19^{+0.06}_{-0.07}$	0.60 ± 0.09	0.50 ± 0.07
3835	$1.59^{+0.12}_{-0.05}$	$10.95^{+0.03}_{-0.04}$	67^{+13}_{-7}	$12.68^{+0.02}_{-0.02}$	668^{+35}_{-35}	$0.63^{+0.02}_{-0.05}$	$11.85^{+0.08}_{-0.09}$	1.07 ± 0.21	7.95 ± 1.54
23490	$1.77^{+0.07}_{-0.08}$	$11.44^{+0.03}_{-0.03}$	138^{+15}_{-14}	$12.23^{+0.05}_{-0.06}$	239^{+31}_{-32}	$-0.19^{+0.05}_{-0.08}$	$11.23^{+0.07}_{-0.08}$	0.72 ± 0.12	0.62 ± 0.10
7630	$1.65^{+0.10}_{-0.11}$	$10.40^{+0.06}_{-0.08}$	56^{+15}_{-13}	$12.16^{+0.08}_{-0.09}$	206^{+43}_{-41}	$0.52^{+0.09}_{-0.11}$	$10.93^{+0.08}_{-0.10}$	0.41 ± 0.08	3.36 ± 0.67
19876	$1.47^{+0.05}_{-0.04}$	$11.31^{+0.02}_{-0.02}$	135^{+17}_{-13}	$12.69^{+0.03}_{-0.03}$	687^{+45}_{-41}	$0.33^{+0.03}_{-0.04}$	<11.20	<0.25	<0.77
8051*	$5.00^{+0.34}_{-0.64}$	$11.34^{+0.06}_{-0.04}$	177^{+69}_{-177}	$12.42^{+0.05}_{-0.07}$	368^{+51}_{-51}	$-0.03^{+0.06}_{-0.11}$	$11.12^{+0.10}_{-0.11}$	0.26 ± 0.06	0.56 ± 0.13

*The 68% confidence interval on BAGPIPES fits of GN-8051's SED using a [S. Charlot & S. M. Fall \(2000\)](#) law includes quiescent galaxy solutions, which are inconsistent with the L_{IR} and M_{mol} measurements. Fitting the same galaxy with a [D. Calzetti et al. \(2000\)](#) law returns $A_V = 2.87$ and $\log M_\star/M_\odot = 10.12$. Assuming this stellar mass implies that GN-8051 is a strongly starbursting galaxy, with $\Delta \text{MS} = 0.96$ dex and $\mu_{\text{mol}} \simeq 10$.

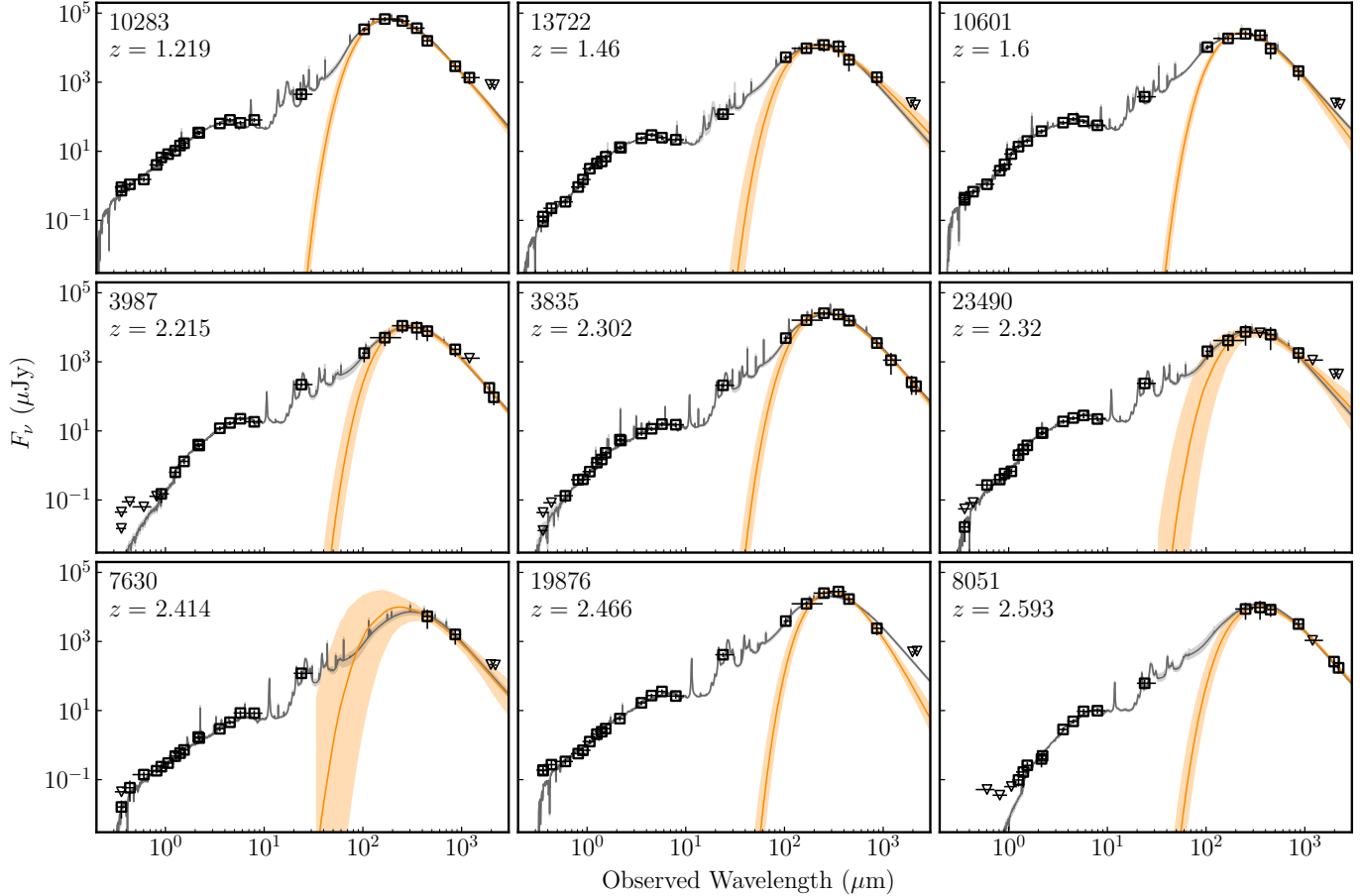


Figure 5. SEDs of the the nine faint DSFGs with spectroscopic redshifts. The CANDELS ID and redshift are shown in the top-left corner of each panel. The gray curve and shaded region in each panel show the median posterior SED and the 16th to 84th percentile range, respectively. The orange curve and shaded region show the median optically-thin MBB SED and the 16th to 84th percentile range, respectively. The square points indicate detections, while the triangles indicate 3σ upper limits. All vertical errorbars show 3σ the measured error.

Table 6. Modified Blackbody SED Fits

ID	T (K)	$\log \frac{L_{\text{IR}}}{L_{\odot}}$	SFR_{KE12} ($M_{\odot} \text{ yr}^{-1}$)	β
(1)	(2)	(3)	(4)	(5)
10283	41^{+5}_{-4}	$12.62^{+0.06}_{-0.05}$	582^{+84}_{-69}	$1.5^{+0.2}_{-0.2}$
13722	50^{+13}_{-9}	$12.01^{+0.08}_{-0.07}$	144^{+30}_{-20}	$0.7^{+0.5}_{-0.4}$
10601	43^{+8}_{-7}	$12.34^{+0.05}_{-0.04}$	312^{+38}_{-31}	$1.2^{+0.5}_{-0.4}$
3987	39^{+38}_{-16}	$12.39^{+0.77}_{-0.47}$	349^{+1698}_{-231}	$1.6^{+0.6}_{-0.4}$
3835	37^{+5}_{-4}	$12.63^{+0.08}_{-0.07}$	596^{+116}_{-85}	$1.7^{+0.3}_{-0.2}$
23490	55^{+41}_{-32}	$12.51^{+0.68}_{-0.67}$	456^{+1748}_{-359}	$1.2^{+1.3}_{-0.7}$
7630	50^{+44}_{-27}	$12.42^{+0.73}_{-0.61}$	367^{+1600}_{-278}	$1.4^{+1.4}_{-0.7}$
19876	33^{+9}_{-6}	$12.63^{+0.09}_{-0.07}$	602^{+140}_{-86}	$2.4^{+0.7}_{-0.7}$
8051	33^{+22}_{-9}	$12.30^{+0.47}_{-0.24}$	279^{+549}_{-119}	$1.5^{+0.4}_{-0.5}$

dest galaxy in this work (see Figure 1), the physical properties that we infer from our BAGPIPES fits are likely biased due to our use of a S. Charlot & S. M. Fall (2000) attenuation law. The 68% confidence interval on SFR_{SED} that is returned by these fits extends to quiescent solutions with $< 1 M_{\odot} \text{ yr}^{-1}$, which is inconsistent with the massive gas reservoir of $\log M_{\text{mol}}/M_{\odot} > 11$ that we inferred from our [C I](1–0) detection, and the high L_{IR} , which implies $\text{SFR}_{\text{KE12}} = 368 \pm 51 M_{\odot} \text{ yr}^{-1}$. When we refit GN-8051’s SED with a D. Calzetti et al. (2000) modified starburst extinction law—keeping all other input models the same—we obtained $A_V = 2.87^{+0.15}_{-0.13}$, with a similar $\text{SFR}_{\text{SED}} = 162^{+30}_{-28} M_{\odot} \text{ yr}^{-1}$ and a much lower stellar mass of only $\log M_{\star}/M_{\odot} = 10.12$.

5.2.3. FIR-Only Modified Blackbody Fits

In addition to the BAGPIPES fits, we performed FIR-only SED fits on our faint DSFG sample following the procedure of S. J. McKay et al. (2023). These fits were motivated by the fact that the shortest wavelength dust emission ($\lambda_{\text{rest}} \leq 40 \mu\text{m}$) can be impacted by AGN heating, whereas the longer-wavelength emission arises almost entirely from star formation-heated dust in the interstellar medium (ISM) (e.g., KE12).

We fit the observed-frame 160 μm to 2 mm fluxes of each galaxy with a MBB template using the Python-based Markov Chain Monte Carlo (MCMC) code emcee (D. Foreman-Mackey et al. 2013). The model has three free parameters: the blackbody temperature, T , the dust emissivity, β , and the overall normalization. The MBB model and fitting procedure² are described in further detail in S. J. McKay et al. (2023). In Figure 5, we show the best-fit MBB SED and 16th to 84th percentile flux interval for each of the nine faint DSFGs in orange, and in Table 6, we provide the median and

16th to 84th percentile posterior values of T and β . We measure blackbody temperatures³ in the range $T = 33 - 55 \text{ K}$ and emissivities in the range $\beta = 0.7 - 2.4$. Both of these are consistent with the typical observed properties of DSFGs in this redshift and $S_{850 \mu\text{m}}$ range (S. J. McKay et al. 2023), though the errors on T are large for galaxies with fewer FIR detections.

As can be seen in Figure 5, the optically thin MBB-only SEDs decline very rapidly in the MIR compared to the BAGPIPES SEDs. To correct for the missing MIR contribution to the 8–1000 μm total IR luminosity, we multiply the integrated luminosities from our MBB fits by a factor of 1.3, following KE12. We provide the corrected L_{IR} for each galaxy in Table 6. We find a range of $\log L_{\text{IR}}/L_{\odot} = 12.0 - 12.6$, with a median of 12.4. These luminosities correspond to $\text{SFR}_{\text{KE12}} \simeq 140 - 600 M_{\odot} \text{ yr}^{-1}$, with a median of $370 M_{\odot} \text{ yr}^{-1}$.

Comparing the infrared luminosities inferred from these MBB fits to those from BAGPIPES, we find a median difference of $\log L_{\text{IR}}^{\text{bagpipes}}/L_{\text{IR}}^{\text{mbb}} = -0.01 \text{ dex}$. The median log difference in L_{IR} for just the four DSFGs containing X-ray AGN (GN-3835, 10283, 10601, and 19876) was slightly higher (+0.05 dex) than for the non-AGN (−0.14 dex), but all of these are smaller than the median measured error on L_{IR} from either fit, suggesting that AGN do not strongly impact the L_{IR} or SFR measurements for our sample.

6. DISCUSSION

We obtained new CO detections for seven faint DSFGs in the GOODS-N, six of which are the first CO detections ever made for these galaxies. To contextualize the results of our survey, we compare the physical properties of our new CO sample (Table 5) with those of CO-detected galaxies at $z = 1 - 3$ from two other large interferometric surveys, namely:

1. The B21 CO detections from ALMA and NOEMA follow-up of ALMA continuum sources, down to $S_{870 \mu\text{m}} = 2 \text{ mJy}$, obtained using a combination of wide-bandwidth linescans (for galaxies with unknown redshifts) and direct targeting of CO at known frequencies, as in this work.
2. CO detections of mostly faint DSFGs from the ASPECS-LP survey (A19), which obtained extremely deep linescans across 5 arcmin² of the Hubble Ultra-Deep Field (HUDF) with contiguous frequency coverage across ALMA Band 3.

In addition to being aimed at detecting CO in relatively faint galaxies, both of these works measured their galaxies’ phys-

² <https://mbb.readthedocs.io/en/latest/>

³ This is different from the characteristic dust temperature T_{d} , which is approximated via Wien’s law, $T_{\text{d}} = (b/\lambda_{\text{peak}})^{1/0.9}$, from which we find our DSFGs have $T_{\text{d}} = 29 - 59 \text{ K}$.

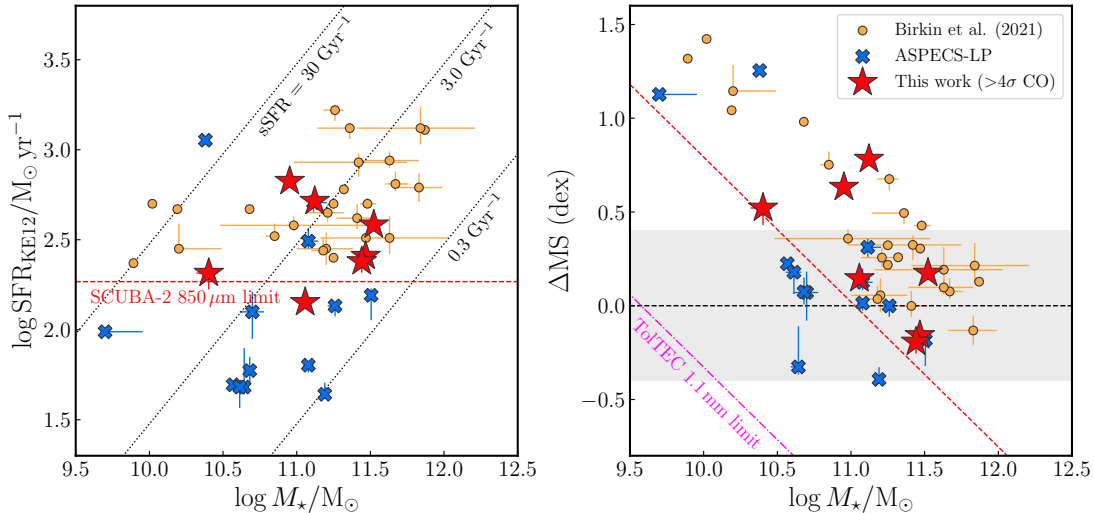


Figure 6. CO-detected DSFGs at $z = 1 - 3$ from this work (red stars), J. E. Birkin et al. (2021) (orange circles), and ASPECS-LP (blue X's). All SFRs were calculated using Equation 8. *Left:* SFR vs. stellar mass. Lines of fixed $\text{sSFR} = \text{SFR}/M_{\star}$ are shown. The approximate SFR corresponding to the confusion limit of SCUBA-2 at $850 \mu \text{m}$ ($185 M_{\odot} \text{ yr}^{-1}$) is shown by the red dashed line. *Right:* Main sequence offset (ΔMS) vs. stellar mass. The black dotted line indicates the J. S. Speagle et al. (2014) SFMS, and a region of $\pm 0.4 \text{ dex}$ around this is shaded grey. The same SFR limit as in the left panel is plotted for $z = 2.5$; low-mass ($M_{\star} \lesssim 10^{11} M_{\odot}$), main-sequence galaxies are excluded from the follow-up CO samples due to the SFR limits of the parent submm samples. The limiting luminosity for TolTEC at 1.1 mm of $L_{\text{IR}} = 10^{11} L_{\odot}$ ($14 M_{\odot} \text{ yr}^{-1}$; N. A. Nava-Moreno et al. 2024), which will enable the selection of galaxies on the SFMS at lower masses, is shown by the magenta dot-dashed line.

ical properties using the MAGPHYS code, which employs similar SED-fitting assumptions as this work, as we discussed in Section 5. To make accurate comparisons across the three samples, we calculated IR-based SFRs for the B21 and A19 galaxies using their L_{IR} values and Equation 8. We limit our comparison to galaxies with $>4\sigma$ CO detections at $z = 1 - 3$, i.e., our seven CO-detected faint DSFGs, 25/50 galaxies from B21, and 13/16 CO-selected galaxies from ASPECS-LP.

We show the SFRs and stellar masses of all three samples in Figure 6, with our CO detections shown by the red stars, B21 galaxies by the orange circles, and ASPECS-LP galaxies by the blue X's. Our CO detections have slightly lower SFRs than the B21 galaxies, as expected given our sample's lower submm flux limits ($S_{850\mu\text{m}} \geq 1.4 \text{ mJy}$ vs. $S_{870\mu\text{m}} \geq 2.0 \text{ mJy}$). The two faintest galaxies in our sample, GN-13722 and GN-7630, have lower SFRs than the entire B21 sample (142 and $206 M_{\odot} \text{ yr}^{-1}$, respectively). The ASPECS-LP galaxies extend to much lower SFRs, down to $\sim 40 M_{\odot} \text{ yr}^{-1}$. Together, the three samples include 45 CO-detected galaxies spanning roughly two orders of magnitude in M_{\star} and SFR, allowing us to investigate the relationships between molecular gas and other physical properties for a wide variety of galaxies using similar assumptions.

6.1. Missing Low- M_{\star} , Main-Sequence DSFGs

The SFRs and stellar masses shown in the left panel of Figure 6 are not tightly correlated, such that the CO detections span a large range of specific star formation rates, $\text{sSFR} \equiv$

SFR/M_{\star} . For reference, we plot black dotted lines of fixed $\text{sSFR} = 0.3, 3.0, \text{ and } 30 \text{ Gyr}^{-1}$ in this panel. This is consistent with recent work showing that faint ($S_{850\mu\text{m}} < 2 \text{ mJy}$) and bright ($>2 \text{ mJy}$) red-selected DSFGs have similar M_{\star} distributions, despite large differences in SFR. (S. J. McKay et al. 2025).

This wide sSFR distribution primarily a consequence of the DSFG population comprising both main-sequence galaxies and starbursting galaxies. This can be seen in the right panel of Figure 6, where we plot the main sequence offsets and stellar masses of the three samples. The main sequence offset is defined as

$$\Delta \text{MS} \equiv \log \left[\frac{\text{SFR}}{\text{SFR}_{\text{MS}}(z, M_{\star})} \right], \quad (9)$$

where SFR_{MS} is the SFR of the SFMS at the redshift and stellar mass of the observed galaxy. We calculated ΔMS assuming the best-fit prescription from J. S. Speagle et al. (2014, their Equation 28), shifted by $+0.03 \text{ dex}$ in M_{\star} to convert to a G. Chabrier (2003) IMF. We selected this fiducial SFMS due to their identical assumed cosmology and calibration to the KE12 L –SFR relations. Critically, this SFMS prescription was also assumed by T20 to measure molecular gas scaling relations (see Section 6.2).

Following A19, we classify galaxies as being on the SFMS if they have $|\Delta \text{MS}| \leq 0.4 \text{ dex}$. Our galaxies have $\Delta \text{MS} = -0.19$ to $+0.78 \text{ dex}$, which we list in Column (7) of Table 5. Three of the nine galaxies (GN-10283, 3835, and 7630) are

starburst galaxies, i.e., above the SFMS, whereas the remaining six⁴ fall on the SFMS. None fall below the SFMS.

Likewise, all of the ASPECS-LP and **B21** galaxies are either on or above the [J. S. Speagle et al. \(2014\)](#) SFMS. We do not reproduce the finding by [A19](#), who used SFRs from MAGPHYS and a [C. Schreiber et al. \(2015\)](#) SFMS, that two of the ASPECS-LP galaxies are below the SFMS. It is worth noting that classifying individual galaxies as on, above, or below the SFMS depends on the assumed SFR method and SFMS prescription, highlighting the importance of a self-consistent approach when comparing galaxy samples.

The right panel of Figure 6 also shows that ΔMS declines with increasing M_* . We interpret this as a selection bias arising from the SFR limits of these surveys: the CO samples from this work and **B21** are submm flux-limited, with all galaxies having $S_{850\mu m}$ (or $S_{870\mu m}$) brighter than the SCUBA-2 confusion limit of 1.4 mJy. This corresponds⁵ to an SFR limit of $185 M_\odot \text{ yr}^{-1}$, which we show with the red dashed lines in Figure 6. The diagonal line in the right panel shows the $\Delta MS - M_*$ relationship corresponding to this fixed SFR for a fixed redshift of $z = 2.5$; because galaxies from submm continuum samples cannot fall below this line, low-mass ($M_* \lesssim 10^{10.5} M_\odot$) DSFGs selected in this way are exclusively starbursts.

6.2. Comparison to Molecular Gas Scaling Relations

While low-mass, main-sequence galaxies are inaccessible to submm-selected surveys such as this work and **B21**, the low-mass, starbursting DSFGs are themselves an interesting population that have been under-represented in previous studies of molecular gas at high redshift.

In particular, relatively few CO detections at $z \gtrsim 1$ with this combination of low M_* and high ΔMS were included in the samples used to measure molecular gas scaling relations (e.g., [R. Genzel et al. 2015](#); [L. J. Tacconi et al. 2018](#); [T20](#)). These studies fit the depletion timescales,

$$t_{\text{dep}} \equiv \frac{M_{\text{mol}}}{\text{SFR}} \quad (10)$$

and the molecular gas fractions,

$$\mu_{\text{mol}} \equiv \frac{M_{\text{mol}}}{M_*} \quad (11)$$

of galaxies as a function of z , M_* , and ΔMS , but the bulk of their CO data are for either $z < 1$ (e.g., [Freundlich et al. 2019](#)) or main-sequence galaxies (e.g., [L. J. Tacconi et al. 2018](#)). The few low-mass, starbursting galaxies that were included in these studies have depletion times and gas fractions

⁴ Including GN-19876 and GN-8051, which were not detected in CO and are not shown in Figure 6.

⁵ Assuming a conversion of $\text{SFR} [M_\odot \text{ yr}^{-1}] = 132 \times S_{850\mu m} [\text{mJy}]$ ([S. J. McKay et al. 2025](#)).

roughly twice as high as the best-fit scaling relations predict (see [L. J. Tacconi et al. 2018](#), their Figure 7).

In this subsection, we compare the depletion times and gas fractions of the three CO samples discussed above to the best-fit [T20](#) scaling relations (their Tables 2 and 3). The properties of these galaxies were measured with similar assumptions to those employed by [T20](#). For consistency, we re-scaled all of the **B21** M_{mol} measurements to $\alpha_{\text{CO}} = 3.6$, which matches our prescription in Section 5.1 and that of [A19](#), as well as the metallicity-based $\alpha_{\text{CO}} = 2 - 5$ used by [T20](#).

6.2.1. Constant Depletion Times

In the left panel of Figure 7, we plot SFR versus M_{mol} for the three CO samples. These properties are tightly correlated, resulting in a small range of depletion times, indicated by the dotted lines of fixed t_{dep} in this panel. We provide t_{dep} for individual galaxies in our sample in Column (9) of Table 5; our galaxies have $t_{\text{dep}} = 210 \text{ Myr}$ to 1.07 Gyr . GN-8051 and GN-19876, which do not have CO detections and therefore are not shown in Figure 7, have short depletion times, with $t_{\text{dep}} = 260 \text{ Myr}$ based on [C I](1–0) in GN-8051, and $t_{\text{dep}} \leq 250 \text{ Myr}$ based on the CO(4–3) upper limit in GN-19876.

[T20](#) find that t_{dep} declines at high z and high ΔMS ; specifically, they measure $t_{\text{dep}, \text{T20}} \propto (1 + z)^{-0.98} (\Delta MS)^{-0.49}$. We plot t_{dep} against z and ΔMS for the three CO samples in the center and right panels of Figure 7, respectively. The green shaded regions in these panels show the best-fit relation from [T20](#) for a wide range of galaxy properties, specified in the caption of Figure 7.

In contrast to the [T20](#) predictions, the depletion times of the CO detections do not appear to evolve with either z or ΔMS . The median (16th-to-84th percentile range) t_{dep} across all three CO samples is 500 (290–850) Myr, with the ASPECS-LP sample having slightly longer t_{dep} (median 630 Myr) compared to our sample (440 Myr) and that of **B21** (460 Myr). The median depletion times of $z < 2$ galaxies (480 Myr) and $z > 2$ galaxies (510 Myr) are consistent with each other, as are those of main-sequence galaxies (520 Myr) and starbursts (450 Myr). Pearson correlation tests likewise suggest there is no correlation between $\log t_{\text{dep}}/\text{yr}$ and $\log(1 + z)$ (Pearson $r = -0.09$, $p = 0.59$) or ΔMS ($r = -0.21$, $p = 0.17$). In summary, our findings are consistent with a constant depletion time of $\sim 500 \text{ Myr}$ across nearly two orders of magnitude in M_{mol} , SFR, and ΔMS .

Because [T20](#) predict much shorter depletion times in starbursts ($t_{\text{dep}} \sim 200 \text{ Myr}$ for $z \sim 2$ and $\Delta MS \sim 1 \text{ dex}$), the starbursting galaxies have the largest offsets from the [T20](#) relation. We measure a mean offset of $\log t_{\text{dep}}/t_{\text{dep}, \text{T20}} = +0.10 \pm 0.04 \text{ dex}$ across all samples and $-0.01 \pm 0.04 \text{ dex}$ in main-sequence galaxies (errors on the mean are from jackknife resampling). However, we measure a mean offset of $+0.33 \pm 0.07 \text{ dex}$ (a factor of 2.1) for just the starbursts, sim-

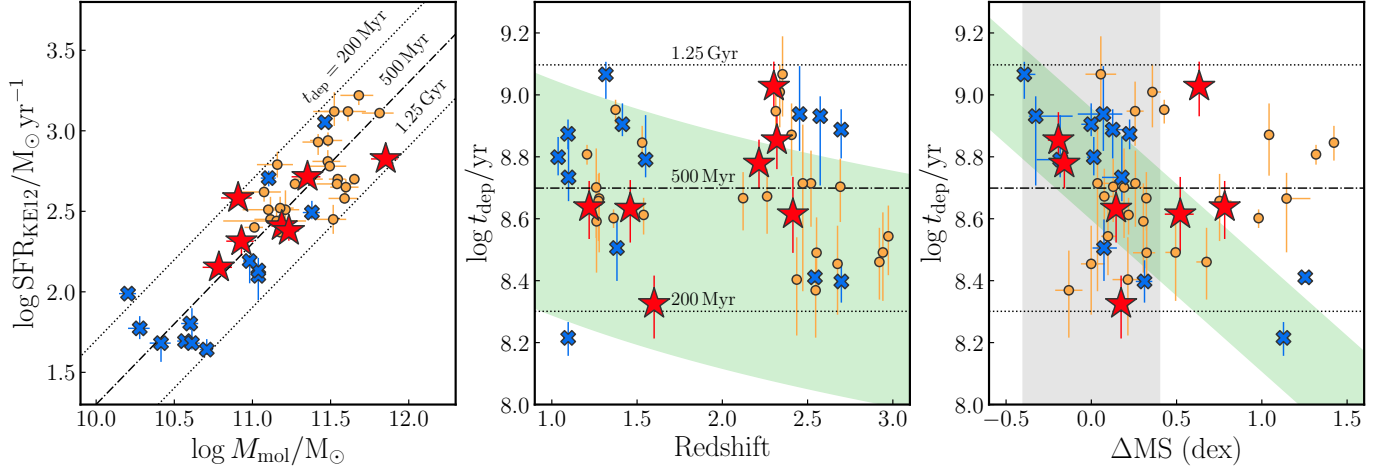


Figure 7. Plots showing the relationship between molecular gas and SFR for $z = 1 - 3$ CO detections. Symbols and colors are the same as in Figure 6. *Left:* SFR vs molecular gas mass. Lines of constant depletion time $t_{\mathrm{dep}} \equiv M_{\mathrm{mol}}/\mathrm{SFR} = 0.2, 0.5$, and 1.25 Gyr are shown. *Middle:* Depletion time vs. redshift. The green shaded region shows the best-fit scaling relation from T20 for a range $M_{\star} = 10^{10-12} M_{\odot}$ and $\Delta \mathrm{MS} = -0.2$ to 1.2 dex (the 5th-to-95th percentile range in $\Delta \mathrm{MS}$ for the galaxies shown). *Right:* Depletion time vs. main sequence offset. The grey shaded region is the same as in Figure 6. The green region shows the best-fit scaling relation from T20, this time for $z = 1 - 3$ and $M_{\star} = 10^{10-12} M_{\odot}$.

ilar to the offsets found in low-mass starbursts by L. J. Tacconi et al. (2018). In Section 6.2.2, we will show that the gas fractions of starbursts are likewise roughly twice as high as the scaling relations predict.

As a final note on the depletion timescale, our measurements of $t_{\mathrm{dep}} \sim 500$ Myr are considerably shorter than the $t_{\mathrm{dep}} \gtrsim 1$ Gyr previously measured by A19. This appears to be due to our use of L_{IR} -based SFRs, which are systematically lower than the SFRs returned directly from SED-fitting codes (MAGPHYS for ASPECS-LP and B21, and BAGPIPES for this work). Direct SED-based SFRs result in median depletion times of 1.28, 0.78, 1.24, and 1.13 Gyr for ASPECS-LP, B21, our sample, and all samples, respectively. Again, this highlights the need for a self-consistent framework when comparing the properties of galaxies from different works.

6.2.2. Higher than Expected Gas Fractions in Starbursts

In contrast to our small range of depletion times, our faint DSFGs exhibit a wide range of molecular gas fractions, $\mu_{\mathrm{mol}} = 0.24 - 7.95$. We provide μ_{mol} for individual faint DSFGs in our sample in Column (10) of Table 5. The ASPECS-LP and B21 CO detections likewise span a large range of μ_{mol} .

We plot μ_{mol} against M_{\star} and $\Delta \mathrm{MS}$ for the three CO samples in the bottom-left and bottom-right panels, respectively, of Figure 8. The symbols are the same as in Figures 6 and 7, but to illustrate better the differences between measured and predicted values of μ_{mol} , we color code the points in the bottom two panels of Figure 8 according to their offsets from the T20 relation—galaxies with μ_{mol} consistent with the relation are colored grey, and galaxies that are more (less) gas-rich

than expected are colored blue (red). Similar to Figure 7, the green shaded regions these panels show the best-fit scaling relation of T20, $\mu_{\mathrm{mol}, \mathrm{T20}} \propto M_{\star}^{-0.41} \Delta \mathrm{MS}^{0.52}$.

The gas fractions of the CO-detected galaxies do increase at lower M_{\star} and higher $\Delta \mathrm{MS}$, as expected, but do so more rapidly than T20 predict. In other words, while massive, main-sequence galaxies fit the T20 relation, starbursting galaxies are more gas-rich than predicted. Specifically, we measure a mean offset $\log \mu_{\mathrm{mol}} / \mu_{\mathrm{mol}, \mathrm{T20}} = +0.13 \pm 0.03$ dex in the main-sequence galaxies, and $\log \mu_{\mathrm{mol}} / \mu_{\mathrm{mol}, \mathrm{T20}} = +0.35 \pm 0.06$ dex (a factor of 2.2) in the starbursts. The latter value is consistent with our finding in Section 6.2.1 that starbursts have t_{dep} 2.1 times longer than predicted.

Figure 8 also shows that galaxies with lower stellar masses are more gas-rich than T20 predict; however, because of the biased relationship between M_{\star} and $\Delta \mathrm{MS}$ (see Section 6.1), it is difficult to determine whether this trend is simply driven by the fact that the low-mass galaxies are also starbursts. We attempted to test this by performing simple linear regressions of $\log \mu_{\mathrm{mol}} / \mu_{\mathrm{mol}, \mathrm{T20}}$, which we show with the purple lines in the top panels of Figure 8. We find a significant correlation (Pearson $r = 0.46, p = 0.0013$) between $\log \mu_{\mathrm{mol}} / \mu_{\mathrm{mol}, \mathrm{T20}}$ and $\Delta \mathrm{MS}$, but only a weak anti-correlation ($r = -0.27, p = 0.08$) between $\log \mu_{\mathrm{mol}} / \mu_{\mathrm{mol}, \mathrm{T20}}$ and $\log M_{\star} / M_{\odot}$. The difference is mainly due to the ASPECS-LP galaxies, which comprise the majority of $M_{\star} < 10^{11} M_{\odot}$ galaxies among the three CO samples, but only two out of 13 starbursts, and are largely consistent with the T20 relations. Further observations of galaxies with $M_{\star} \sim 10^{10} M_{\odot}$ both on and above the SFMS will be necessary to accurately measure the evolution of μ_{mol} with both M_{\star} and $\Delta \mathrm{MS}$.

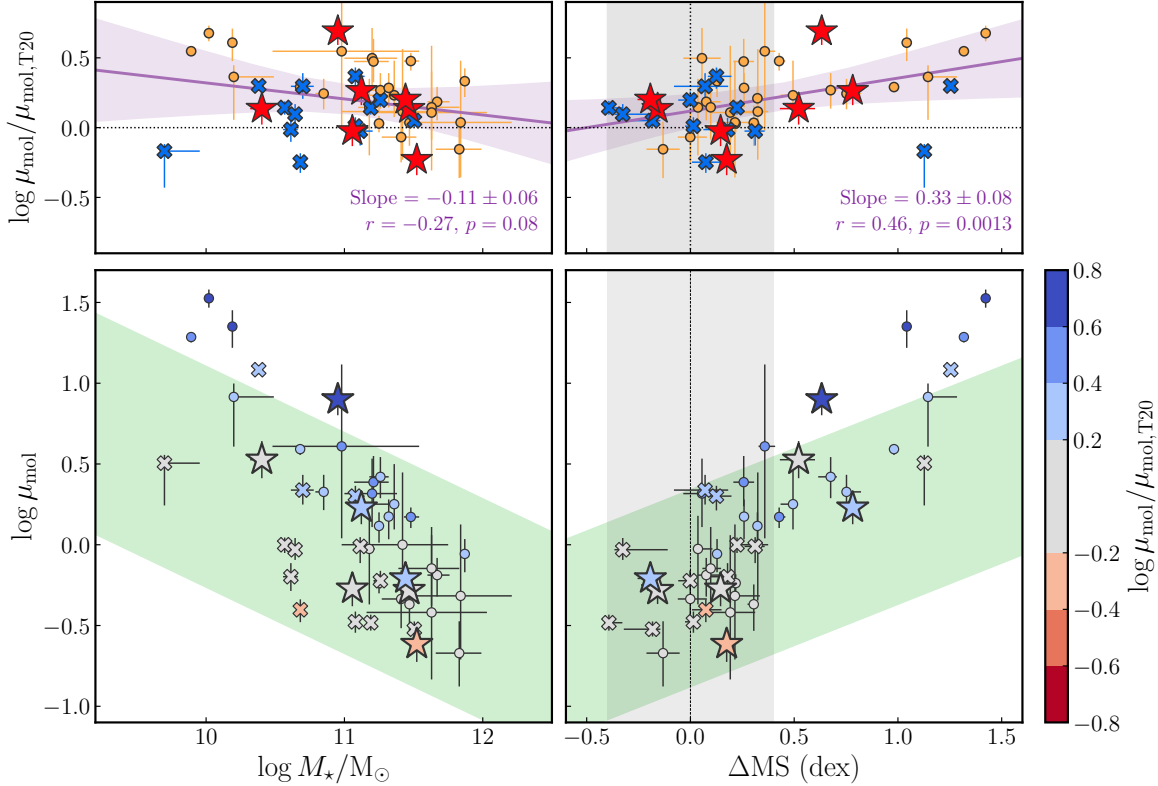


Figure 8. Relationships between molecular gas fraction, $\mu_{\text{mol}} = M_{\text{mol}}/M_{\star}$, and galaxy physical properties. Symbols are the same as in Figures 6 and 7, but colors in the bottom two panels now show offsets of μ_{mol} from the best-fit T20 scaling relation—grey points are within the 0.2 dex scatter of this relation, while blue (red) colors indicate galaxies that are more (less) gas-rich than predicted. The black dashed line and grey shaded region again indicate the J. S. Speagle et al. (2014) SFMS and a range $\Delta\text{MS} = -0.4$ to 0.4 dex, respectively. *Bottom left:* Gas fraction vs. stellar mass. The green shaded region shows the T20 relation for $z = 1 - 3$ and $\Delta\text{MS} = -0.2$ to 1.2 dex. *Bottom right:* Gas fraction vs. main sequence offset. The green shaded region shows the T20 relation for $z = 1 - 3$ and $M_{\star} = 10^{10-12} M_{\odot}$. *Top panels:* Offsets of the measured gas fractions from the predicted values of T20 vs. stellar mass and main sequence offset. The horizontal dotted lines indicate $\log \mu_{\text{mol}}/\mu_{\text{mol,T20}} = 0$. The purple lines show the best-fit linear relationships between these variables, with 3σ errors on this fit shaded purple. The best-fit slope, Pearson r statistic, and p value for the linear correlation are shown in the bottom right corner.

6.2.3. Evidence for Evolving α_{CO} ?

The factor of ≈ 2 higher t_{dep} and μ_{mol} in low-mass and starbursting galaxies than predicted by the T20 scaling relations may indicate that these relations do not hold for low-mass starbursts. However, this may also indicate that M_{mol} is systematically overestimated in this population, i.e., by not accounting for the stellar mass- or sSFR-dependence of α_{CO} and/or CO excitation. Although a full analysis of these effects is outside the scope of this work, we briefly comment on these possible factors below.

First, α_{CO} is known to vary widely depending on ISM conditions that can be correlated with both M_{\star} and ΔMS (see, e.g., the review by A. D. Bolatto et al. 2013). The observed t_{dep} and μ_{mol} offsets could be accounted for by a lower CO-to-H₂ conversion factor, $\alpha_{\text{CO}} \sim 1 - 2$, in the starburst galaxies (e.g., B. Magnelli et al. 2012; M. S. Bothwell et al. 2013). Notably, applying a metallicity correction to α_{CO} (e.g., R. Genzel et al. 2012, 2015; L. J. Tacconi et al. 2018) by assuming a mass-metallicity relation would *worsen* the deviations,

since this would increase α_{CO} in the low-mass galaxies and decrease α_{CO} in the more massive galaxies that already fit the T20 relations. A more nuanced approach to α_{CO} assumptions is necessary.

The CO in these galaxies could also be more excited, such that the luminosities of the detected $J_{\text{up}} \geq 2$ CO lines correspond to lower $L'_{\text{CO}(1-0)}$ values. D. A. Riechers et al. (2020) found that assumptions about CO excitation alone could bias molecular gas mass estimates systematically by up to a factor of 2. M. Frias Castillo et al. (2023) did not find evidence for correlation between CO excitation and galaxy properties including SFR surface density, but their sample was limited to very bright DSFGs with $S_{850\mu\text{m}} > 10 \text{ mJy}$ at $z = 2 - 5$.

Finally, the selection biases in the left panel of Figure 6 make disentangling the joint effect of M_{\star} and ΔMS on α_{CO} and the CO SLED difficult. Further CO observations in DSFGs both on and above the SFMS, as well as a careful approach to measuring physical properties consistently, are needed.

6.3. Red Selection for CO in Low- M_* Main Sequence DSFGs

In Section 6.1, we showed that sensitivity limits of submm/mm continuum surveys prevent the selection of DSFGs on the SFMS at $\lesssim 10^{11} M_\odot$ for follow-up CO observations. This is problematic, given the expense of blind surveys like ASPECS-LP. Intentionally targeting main sequence galaxies (e.g., L. J. Tacconi et al. 2013; R. Genzel et al. 2015) at low mass from submm parent samples will require substantially deeper continuum observations.

The flux limits (and thus SFR limits) of single-dish submm/mm surveys will be vastly improved by sensitive cameras on larger telescopes than the 15-m JCMT, such as the NIKA2 camera on the IRAM 30-m Telescope (e.g., L. Bing et al. 2023), or the TolTEC camera on the Large Millimeter Telescope (LMT; Wilson et al. 2020). The TolTEC survey of the UDS, for example, has an anticipated 4σ detection threshold of $L_{\text{IR}} \sim 10^{11} L_\odot$ (N. A. Nava-Moreno et al. 2024), or $\text{SFR} \sim 14 M_\odot \text{ yr}^{-1}$ using Equation 8—over an order of magnitude lower than that of SCUBA-2 at 850 μm . We plot this limit for $z = 2.5$ as a magenta dot-dashed line in Figure 6, which shows that instruments like TolTEC will enable the targeted follow-up of large samples of low-mass ($\log M_*/M_\odot \gtrsim 9 - 9.5$) main sequence DSFGs around cosmic noon for the first time. Importantly, while some mosaicked interferometric continuum surveys can achieve similar sensitivities (e.g., J. González-López et al. 2020), the large areas covered by single-dish surveys are necessary to minimize bias due to cosmic variance.

Intentionally targeting low-mass DSFGs both on and above the SFMS will require accurate counterpart matching between the submm/mm sources and their OIR counterparts. At a minimum, any method used for counterpart selection must have better spatial resolution than the submm/mm continuum imaging, and it must select at least as many galaxies as the number of submm/mm sources. These requirements make most existing methods of counterpart selection unusable for the next generation of submm/mm surveys.

For the TolTEC UDS survey, the expected surface density of submm/mm detections above their $L_{\text{IR}} \sim 10^{11} L_\odot$ threshold is $\sim 10 \text{ arcmin}^{-2}$, and the spatial resolution of TolTEC at 1.1 mm is $\sim 5''$ (N. A. Nava-Moreno et al. 2024). Radio counterparts (3.1 arcmin^{-2} for $S_{1.4\text{GHz}} > 11 \mu\text{Jy}$; F. Owen 2018) and the F160W–IRAC2 red selection used in this work ($\sim 5 \text{ arcmin}^{-2}$) do not provide enough galaxies to account for the stellar counterparts of these sources. MIR point sources are more numerous (16 arcmin^{-2} ; D. Elbaz et al. 2011), but the spatial resolution of Spitzer/MIPS at 24 μm is not an improvement over that of TolTEC itself. The best option for identifying the stellar counterparts of the faintest DSFGs may instead be NIRCam-based red selection (A. J. Barger & L. L. Cowie 2023), since NIRCam imaging in deep legacy fields,

such as the GOODS-N, is already ~ 3 mag deeper at 1.5 μm and ~ 5.5 mag deeper at 4.5 μm than the equivalent HST and *Spitzer* filters (D. J. Eisenstein et al. 2023).

7. SUMMARY

We presented our NOEMA survey of CO(3–2) and CO(4–3) in eight DSFGs near the SCUBA-2 confusion limit ($S_{850\mu\text{m}} = 1.4 - 3.5 \text{ mJy}$) in the CANDELS GOODS-N field. We selected the HST counterparts to these galaxies using a HST/Spitzer NIR flux-color cut, and we limited the sample to galaxies with existing spectroscopic redshifts from the literature. This allowed us to target the CO (or [C I]) line in each galaxy with a single NOEMA frequency tuning. Seven out of our eight targets were detected in CO at a $> 5\sigma$ significance at the expected frequency based on their OIR redshifts. We additionally detected the 2 mm continuum in two of our targets, as well as in two serendipitous off-axis DSFGs, one of which was also detected in [C I](1–0).

We derived molecular gas masses from each of the emission lines, performed UV-to-mm SED fits to measure L_{IR} and M_* for our sample, and calculated SFRs assuming the SFR– L_{IR} conversion from KE12. Finally, we compared the results for our faint DSFG sample, along with those for two other faint, CO-detected DSFG samples at $z = 1 - 3$ from the literature, to the SFMS of J. S. Speagle et al. (2014) and the molecular gas scaling relations from T20. Our conclusions from this work are as follows:

1. Our NIR color selection of $f_{4.5\mu\text{m}}/f_{\text{F160W}} > 3.5$ and $f_{4.5\mu\text{m}} > 1 \mu\text{Jy}$ correctly identified the OIR counterparts for seven of our eight NOEMA targets, which is consistent with the $\sim 90\%$ accuracy of similar selections in the literature.
2. Our intentional selection of the faintest SCUBA-2 sources in the GOODS-N allowed us to detect CO in galaxies with lower SFRs than those in similar follow-up surveys with NOEMA and ALMA.
3. The DSFGs in this work, both from our survey and from the two literature samples, are all classified as either main sequence galaxies or starburst galaxies based on the assumptions used in this work. We caution that comparisons of DSFGs across surveys, especially their offsets from the SFMS, requires careful consideration of the SFMS and SFR prescriptions used.
4. Due to the direct relationship between submm flux and SFR, follow-up CO surveys derived from submm flux-limited parent samples display a selection bias, such that low-mass ($M_* \lesssim 10^{11} M_\odot$) galaxies on the main sequence are absent from these samples.
5. Galaxies on the SFMS at $z = 1 - 3$ have depletion timescales and molecular gas fractions consistent with

molecular gas scaling relations from L. J. Tacconi et al. (2020), but low-mass, starbursting DSFGs have depletion timescales and gas fractions a median of two times higher than predicted, which may be evidence for lower α_{CO} and/or higher CO excitation in these galaxies.

6. Disentangling the M_{\star} - and ΔMS -dependences of α_{CO} and the CO SLED will require further observations of CO in DSFGs on and above the SFMS, which may be identified via a NIRCam-based selection.

Facilities: JCMT (SCUBA-2), NOEMA, Keck-I (LRIS, MOSFIRE), HST (ACS, WFC3), SMA, VLA, Subaru (SuprimeCam), CFHT (WIRCam), Herschel (SPIRE), Spitzer (IRAC).

Software: astropy (Astropy Collaboration et al. 2013, 2018, 2022); GILDAS (Gildas Team 2013); numpy (Harris et al. 2020); scipy (Virtanen et al. 2020)

1 This work is based on observations carried out un-
 2 der project numbers W23CH and S24BR with the
 3 IRAM NOEMA Interferometer. IRAM is supported by
 4 INSU/CNRS (France), MPG (Germany) and IGN (Spain).
 5 M.J.N.R. thanks our IRAM contacts, Kirsty May Butler and
 6 Romane Le Gal, for valuable assistance in the reduction of
 7 these NOEMA data.

8 The James Clerk Maxwell Telescope is operated by the
 9 East Asian Observatory on behalf of The National Astronom-
 10 ical Observatory of Japan; Academia Sinica Institute of As-
 11 tronomy and Astrophysics; the Korea Astronomy and Space
 12 Science Institute; the National Astronomical Research In-
 13 stitute of Thailand; Center for Astronomical Mega-Science
 14 (as well as the National Key R&D Program of China with
 15 No. 2017YFA0402700). Additional funding support is pro-
 16 vided by the Science and Technology Facilities Council of
 17 the United Kingdom and participating universities and orga-
 18 nizations in the United Kingdom and Canada.

REFERENCES

Alexander, D. M., Bauer, F. E., Brandt, W. N., et al. 2003, AJ, 126, 2, 539.
 doi:10.1086/376473

Aravena, M., Decarli, R., Gómez-López, J., et al. 2019, ApJ, 882, 2, 136.
 doi:10.3847/1538-4357/ab30df

Astropy Collaboration, Robitaille, T. P., Tollerud, E. J., et al. 2013, A&A, 558, A33. doi:10.1051/0004-6361/201322068

Astropy Collaboration, Price-Whelan, A. M., Sipőcz, B. M., et al. 2018, AJ, 156, 3, 123. doi:10.3847/1538-3881/aabc4f

Astropy Collaboration, Price-Whelan, A. M., Lim, P. L., et al. 2022, ApJ, 935, 2, 167. doi:10.3847/1538-4357/ac7c74

Barger, A. J., Cowie, L. L., & Wang, W.-H. 2008, ApJ, 689, 2, 687.
 doi:10.1086/592735

Barger, A. J., Wang, W.-H., Cowie, L. L., et al. 2012, ApJ, 761, 2, 89.
 doi:10.1088/0004-637X/761/2/89

Barger, A. J., Cowie, L. L., Chen, C.-C., et al. 2014, ApJ, 784, 1, 9.
 doi:10.1088/0004-637X/784/1/9

Barger, A. J. & Cowie, L. L. 2023, ApJ, 956, 2, 95.
 doi:10.3847/1538-4357/acedaa

Barro, G., Pérez-González, P. G., Cava, A., et al. 2019, ApJS, 243, 2, 22.
 doi:10.3847/1538-4365/ab23f2

Barrufet, L., Dunlop, J. S., Begley, R., et al. 2025, , arXiv:2508.05740.
 doi:10.48550/arXiv.2508.05740

Berta, S., Lagache, G., Beelen, A., et al. 2025, A&A, 696, A193.
 doi:10.1051/0004-6361/202452894

Bing, L., Béthermin, M., Lagache, G., et al. 2023, A&A, 677, A66.
 doi:10.1051/0004-6361/202346579

Birkin, J. E., Weiss, A., Wardlow, J. L., et al. 2021, MNRAS, 501, 3, 3926.
 doi:10.1093/mnras/staa3862

Blain, A. W., Ivison, R. J., & Smail, I. 1998, MNRAS, 296, 3, L29.
 doi:10.1046/j.1365-8711.1998.01605.x

Bolatto, A. D., Wolfire, M., & Leroy, A. K. 2013, ARA&A, 51, 1, 207.
 doi:10.1146/annurev-astro-082812-140944

Bothwell, M. S., Smail, I., Chapman, S. C., et al. 2013, MNRAS, 429, 4, 3047. doi:10.1093/mnras/sts562

Bruzual, G. & Charlot, S. 2003, MNRAS, 344, 4, 1000.
 doi:10.1046/j.1365-8711.2003.06897.x

Calzetti, D., Armus, L., Bohlin, R. C., et al. 2000, ApJ, 533, 2, 682.
 doi:10.1086/308692

Carnall, A. C., McLure, R. J., Dunlop, J. S., et al. 2018, MNRAS, 480, 4, 4379. doi:10.1093/mnras/sty2169

Carnall, A. C., Leja, J., Johnson, B. D., et al. 2019, ApJ, 873, 1, 44.
 doi:10.3847/1538-4357/ab04a2

Casey, C. M. 2012, MNRAS, 425, 4, 3094.
 doi:10.1111/j.1365-2966.2012.21455.x

Chabrier, G. 2003, PASP, 115, 809, 763. doi:10.1086/376392

Chapman S. C., Blain A. W., Smail I., & Ivison R. J., 2005, ApJ, 622, 2, 772. doi:10.1086/428082

Charlot, S. & Fall, S. M. 2000, ApJ, 539, 2, 718. doi:10.1086/309250

Chen, C.-C., Cowie, L. L., Barger, A. J., et al. 2013, *ApJ*, 762, 2, 81. doi:10.1088/0004-637X/762/2/81

Cowie, L. L., Barger, A. J., Hsu, L.-Y., et al. 2017, *ApJ*, 837, 2, 139. doi:10.3847/1538-4357/aa60bb

Cowie, L. L., González-López, J., Barger, A. J., et al. 2018, *ApJ*, 865, 2, 106. doi:10.3847/1538-4357/aadc63

Cowie, L. L., Barger, A. J., Bauer, F. E., et al. 2022, *ApJ*, 939, 1, 5. doi:10.3847/1538-4357/ac91d2

da Cunha, E., Charlton, S., & Elbaz, D. 2008, *MNRAS*, 388, 4, 1595. doi:10.1111/j.1365-2966.2008.13535.x

da Cunha, E., Walter, F., Smail, I. R., et al. 2015, *ApJ*, 806, 1, 110. doi:10.1088/0004-637X/806/1/110

Daddi, E., Bournaud, F., Walter, F., et al. 2010, *ApJ*, 713, 1, 686. doi:10.1088/0004-637X/713/1/686

Daddi, E., Dannerbauer, H., Liu, D., et al. 2015, *A&A*, 577, A46. doi:10.1051/0004-6361/201425043

Draine, B. T. & Li, A. 2007, *ApJ*, 657, 2, 810. doi:10.1086/518306

Dunne, L., Maddox, S. J., Papadopoulos, P. P., et al. 2022, *MNRAS*, 517, 1, 962. doi:10.1093/mnras/stac2098

Eisenstein, D. J., Willott, C., Alberts, S., et al. 2023, arXiv:2306.02465. doi:10.48550/arXiv.2306.02465

Elbaz, D., Dickinson, M., Hwang, H. S., et al. 2011, *A&A*, 533, A119. doi:10.1051/0004-6361/201117239

Engel, H., Tacconi, L. J., Davies, R. I., et al. 2010, *ApJ*, 724, 1, 233. doi:10.1088/0004-637X/724/1/233

Foreman-Mackey, D., Hogg, D. W., Lang, D., et al. 2013, *PASP*, 125, 925, 306. doi:10.1086/670067

Frayer, D. T., Koda, J., Pope, A., et al. 2008, *ApJL*, 680, 1, L21. doi:10.1086/589830

Freundlich, J., Combes, F., Tacconi, L. J., et al. 2019, *A&A*, 622, A105. doi:10.1051/0004-6361/201732223

Frias Castillo, M., Hodge, J., Rybak, M., et al. 2023, *ApJ*, 945, 2, 128. doi:10.3847/1538-4357/acb931

Genzel, R., Tacconi, L. J., Combes, F., et al. 2012, *ApJ*, 746, 1, 69. doi:10.1088/0004-637X/746/1/69

Genzel, R., Tacconi, L. J., Lutz, D., et al. 2015, *ApJ*, 800, 1, 20. doi:10.1088/0004-637X/800/1/20

Giavalisco, M., Ferguson, H. C., Koekemoer, A. M., et al. 2004, *ApJ*, 600, 2, L93. doi:10.1086/379232

Gildas Team 2013, Astrophysics Source Code Library. ascl:1305.010

González-López, J., Novak, M., Decarli, R., et al. 2020, *ApJ*, 897, 1, 91. doi:10.3847/1538-4357/ab765b

Greve, T. R., Bertoldi, F., Smail, I., et al. 2005, *MNRAS*, 359, 3, 1165. doi:10.1111/j.1365-2966.2005.08979.x

Greve, T. R., Leonidaki, I., Xilouris, E. M., et al. 2014, *ApJ*, 794, 2, 142. doi:10.1088/0004-637X/794/2/142

Grogan, N. A., Kocevski, D. D., Faber, S. M., et al. 2011, *ApJS*, 197, 2, 35. doi:10.1088/0067-0049/197/2/35

Harris, C. R., Millman, K. J., van der Walt, S. J., et al. 2020, *Nature*, 585, 7825, 357. doi:10.1038/s41586-020-2649-2

Hodge, J. A., Swinbank, A. M., Simpson, J. M., et al. 2016, *ApJ*, 833, 1, 103. doi:10.3847/1538-4357/833/1/103

Högberg, J. A. 1974, *A&AS*, 15, 417.

Holland, W. S., Bintley, D., Chapin, E. L., et al. 2013, *MNRAS*, 430, 4, 2513. doi:10.1093/mnras/sts612

Hsu, L.-Y., Cowie, L. L., Chen, C.-C., et al. 2016, *ApJ*, 829, 1, 25. doi:10.3847/0004-637X/829/1/25

Hsu, Q.-N., Cowie, L. L., Chen, C.-C., et al. 2024, *ApJL*, 964, 2, L32. doi:10.3847/2041-8213/ad3421

Jiao, Q., Zhao, Y., Zhu, M., et al. 2017, *ApJL*, 840, 2, L18. doi:10.3847/2041-8213/aa6f0f

Kaufman, M. J., Wolfire, M. G., Hollenbach, D. J., et al. 1999, *ApJ*, 527, 2, 795. doi:10.1086/308102

Kennicutt, R. C. 1998, *ApJ*, 498, 2, 541. doi:10.1086/305588

Kennicutt, R. C. & Evans, N. J. 2012, *ARA&A*, 50, 531. doi:10.1146/annurev-astro-081811-125610

Kodra, D., Andrews, B. H., Newman, J. A., et al. 2023, *ApJ*, 942, 1, 36. doi:10.3847/1538-4357/ac9f12

Koekemoer, A. M., Faber, S. M., Ferguson, H. C., et al. 2011, *ApJS*, 197, 2, 36. doi:10.1088/0067-0049/197/2/36

Kriek, M., Shapley, A. E., Reddy, N. A., et al. 2015, *ApJS*, 218, 2, 15. doi:10.1088/0067-0049/218/2/15

Liu, D., Gao, Y., Isaak, K., et al. 2015, *ApJL*, 810, 2, L14. doi:10.1088/2041-8205/810/2/L14

Madau, P. & Dickinson, M. 2014, *ARA&A*, 52, 415. doi:10.1146/annurev-astro-081811-125615

Magnelli, B., Saintonge, A., Lutz, D., et al. 2012, *A&A*, 548, A22. doi:10.1051/0004-6361/201220074

McLean, I. S., Steidel, C. C., Epps, H. W., et al. 2012, *Proc. SPIE*, 8446, 84460J. doi:10.1117/12.924794

McKay, S. J., Barger, A. J., Cowie, L. L., et al. 2023, *ApJ*, 951, 1, 48. doi:10.3847/1538-4357/acde1e5

McKay, S. J., Barger, A. J., & Cowie, L. L. 2024, *ApJ*, 962, 2, 128. doi:10.3847/1538-4357/ad1e61

McKay, S. J., Barger, A. J., Cowie, L. L., et al. 2025, *ApJ*, 988, 1, 135. doi:10.3847/1538-4357/ade394

Nava-Moreno, N. A., Montaña, A., Aretxaga, I., et al. 2024, *MNRAS*, 531, 4, 4900. doi:10.1093/mnras/stae1417

Nicandro Rosenthal, M. J., Barger, A. J., Cowie, L. L., et al. 2025, *ApJ*, 979, 2, 247. doi:10.3847/1538-4357/ad9c67

Owen, F. N. 2018, *ApJS*, 235, 2, 34. doi:10.3847/1538-4365/aab4a1

Pacífici, C., da Cunha, E., Charlton, S., et al. 2015, *MNRAS*, 447, 1, 786. doi:10.1093/mnras/stu2447

Pope, A., Scott, D., Dickinson, M., et al. 2006, *MNRAS*, 370, 3, 1185. doi:10.1111/j.1365-2966.2006.10575.x

Pope, A., Chary, R.-R., Alexander, D. M., et al. 2008, *ApJ*, 675, 2, 1171. doi:10.1086/527030

Riechers, D. A., Boogaard, L. A., Decarli, R., et al. 2020, *ApJL*, 896, 2, L21. doi:10.3847/2041-8213/ab9595

Schmidt, M. 1959, *ApJ*, 129, 243. doi:10.1086/146614

Schreiber, C., Pannella, M., Elbaz, D., et al. 2015, *A&A*, 575, A74. doi:10.1051/0004-6361/201425017

Solomon, P. M. & Vanden Bout, P. A. 2005, *ARA&A*, 43, 1, 677. doi:10.1146/annurev.astro.43.051804.102221

Speagle, J. S., Steinhardt, C. L., Capak, P. L., et al. 2014, *ApJS*, 214, 2, 15. doi:10.1088/0067-0049/214/2/15

Swinbank, A. M., Smail, I., Chapman, S. C., et al. 2004, *ApJ*, 617, 1, 64. doi:10.1086/425171

Tacconi, L. J., Neri, R., Genzel, R., et al. 2013, *ApJ*, 768, 1, 74. doi:10.1088/0004-637X/768/1/74

Tacconi, L. J., Genzel, R., Saintonge, A., et al. 2018, *ApJ*, 853, 2, 179. doi:10.3847/1538-4357/aaa4b4

Tacconi, L. J., Genzel, R., & Sternberg, A. 2020, *ARA&A*, 58, 157. doi:10.1146/annurev-astro-082812-141034

Virtanen, P., Gommers, R., Oliphant, T. E., et al. 2020, *Nature Methods*, 17, 261. doi:10.1038/s41592-019-0686-2

Walter, F., Decarli, R., Aravena, M., et al. 2016, *ApJ*, 833, 1, 67. doi:10.3847/1538-4357/833/1/67

Wang, T., Elbaz, D., Schreiber, C., et al. 2016, *ApJ*, 816, 2, 84. doi:10.3847/0004-637X/816/2/84

Wang, T., Schreiber, C., Elbaz, D., et al. 2019, *Nature*, 572, 7768, 211. doi:10.1038/s41586-019-1452-4

Wilson, G. W., Abi-Saad, S., Ade, P., et al. 2020, *Proc. SPIE*, 11453, 1145302. doi:10.1117/12.2562331

Wirth, G. D., Trump, J. R., Barro, G., et al. 2015, *AJ*, 150, 5, 153. doi:10.1088/004-6256/150/5/153

Xue, Y. Q., Luo, B., Brandt, W. N., et al. 2016, *ApJS*, 224, 2, 15. doi:10.3847/0067-0049/224/2/15

Zavala, J. A., Casey, C. M., Manning, S. M., et al. 2021, *ApJ*, 909, 2, 165. doi:10.3847/1538-4357/abdb27